UNIVERSITÀ DEGLI STUDI DI PADOVA

Dipartimento di Fisica e Astronomia "Galileo Galilei"

Corso di Laurea Magistrale in Fisica

Tesi di Laurea

Test of a ^{3}He target to be used for transfer reactions in inverse kinematics and study of the nuclear structure of ^{74}Se

Relatori

Dr. Daniele Mengoni

Dr. Jose Javier Valiente-Dobón

Dr. Marco Siciliano

Laureando

Gabriele Carozzi

Anno Accademico 2017/2018

Abstract

In the last years, in the field of nuclear physics, great efforts have been made to produce and study nuclei far from the valley of stability. This has prompted the construction of facilities that produce Radioactive Ion Beams to push our knowledge to the limits of nuclear existence. One way to make use of these beams is via direct reactions (such as transfer reactions), which require new targets of light nuclei. These reactions need to be performed in inverse kinematics, as the heavier nuclei that are involved are unstable: they can be accelerated to form beams, but they do not live long enough to make targets out of them. Among these light nuclei, ^{3}He is one of the most promising choices for the study of neutron-deficient nuclei, as it can be used in two-proton transfer reactions. For this purpose a solid, thin target of ^{nat}W with ^{3}He absorbed in the metallic lattice has been produced with an innovative technique (to be patented) in a collaboration between the Legnaro National Laboratories (LNL), Italy, and the CSIC-Materials Science Institute of Seville, Spain. The target has been tested at the LNL with a beam of stable ^{64}Zn; the GALILEO γ-ray array, the Neutron-Wall neutron detector and the EUCLIDES light charged particle detector were employed to study the reaction. In this work, the target and its properties are described, and the complete analysis of the data collected during the test experiment is presented. This includes not only the results of the test itself, but also the study of the feasibility of neutron angular distributions measurement with the Neutron-Wall detector. Moreover, in fusion evaporation reactions with contaminants present in the target ^{74}Se was produced abundantly: this allowed the study of its nuclear structure.

Contents

Chapter 1

Introduction

In the last years, in the field of nuclear physics, there has been a large interest in the study of exotic nuclei far from stability, which allow the study of the nuclear hamiltonian in a new and challenging context. This quest prompted the development of innovative research facilities that employ radioactive ion beams (RIBs). One example of these new endeavors is the SPES facility at the Legnaro National Laboratories (LNL), Italy. In order to go beyond our current knowledge of the nuclear structure near the valley of stability, new targets of light nuclei (such as d, ^{3}He, etc.), to be used for proton transfer reactions in inverse kinematics, are of utmost importance. Especially when used together with already neutron-deficient ion beams, they allow the population of nuclei very close to the proton dripline.

For this purpose, an innovative ^{3}He solid target has been developed in a collaboration between the LNL and the CSIC-Materials Science Institute of Seville, Spain [1]. The main aim is to use this target in experiments that populate low-lying states in the nuclei of interest via the two-proton transfer reaction (^{3}He,n), and measure their lifetimes via the Doppler Shift Attenuation Method (DSAM) [2].

In this thesis, the test of such target is presented. The test experiment was performed at the LNL with an incident beam of ^{64}Zn at an energy of 275 MeV; the allotted beam time was 24 hours. The nucleus of interest was the ^{66}Ge, populated via the two-proton transfer reaction ^{64}Zn(^{3}He,n)^{66}Ge in inverse kinematics. In the experiment, the GALILEO [3] γ-ray array was used in conjunction with the Neutron-Wall [4] neutron detector and the EUCLIDES [5] light charged particle detector. Moreover, for the first time, the feasibility of neutron angular distribution measurements with Neutron-Wall was studied.

1.1 Transfer reactions in inverse kinematics

The ultimate goal with this target is to study the structure of neutron-deficient nuclei via lifetime measurements. In particular, the main interest is to populate and study low-energy, low-angular momentum states. In this context, transfer reactions are the most useful ones to be used, as they are very selective [6, 7]: the distribution of angular momentum carried by the transferred particles is really narrow, and low-momentum transfer is favored. Moreover, the value of angular momentum that is more likely to be transferred depends on the energy of the projectile.

These properties can be obtained from in-depth theoretical analysis of transfer reactions, which has been done in the past by F. Zardi [7]. In the following, some of the details of his approach are presented.
At very high energies over the Coulomb barrier, as in the case of the test experiment discussed in this work, the trajectory of the projectile relative to the target can be considered rectilinear (in principle this assumption can be made even at lower energies, as long as the transferred energy is lower than the total kinetic energy). In addition to this, the probability of transfer becomes relevant only at grazing trajectories, when the impact parameter is comparable to the sum of the radii of the target and the projectile: if it is too low, other reaction channels become more relevant; if it is too high, the wavefunction of the nucleon that is transferred is too low and the transfer probability goes to zero. This condition effectively describes a ring around the target nucleus where the transfer reaction can take place. Moreover, given the same conditions, a transfer reaction is more likely to happen the smoother the transition between initial and final trajectories is.

When these conditions are taken into account, the main properties of the reaction in the case of one nucleon transfer can be derived by considering the approximate conservation of energy and angular momentum of the transferred particle.
The nucleon is initially bound to the projectile with binding energy E_i, and has average kinetic energy $\frac{1}{2}Mv^2$, (M is the mass of the nucleon, v is the velocity of the projectile). After being transferred on the target, the nucleon is bound to the target with binding energy E_f, while the projectile moves on with roughly the same velocity as before, but with energy lowered by $\sim \frac{1}{2}Mv^2$. For the transferred particle, the energy balance can be expressed as

$$E_f \simeq E_i + \frac{1}{2}Mv^2 \tag{1.1}$$

Now, the Q-value of the reaction is $E_i - E_f$, therefore

$$Q \simeq -\frac{1}{2}Mv^2 \tag{1.2}$$

Therefore, final states with energy E_f that follow equation 1.2 are more likely to be populated. The reaction is always endothermic, and the most populated states in the final nucleus have higher energy the higher the energy of the collision is.
As for the angular momentum, first a grazing collision is considered: when the transfer takes place, the nucleon is on the surface of the projectile, at a distance R_T from the center of the target, and is moving with average velocity v. The value of angular momentum that is more likely to be transferred is then

$$\hbar l \simeq MvR_T \tag{1.3}$$

When the transfer occurs with the condition described above, the angular momentum in the final nucleus is perpendicular to the scattering plane:

$$l_Z = l \tag{1.4}$$

If more than one nucleon is transferred, at these energies the mechanism can be interpreted as if all the particles are transferred at once. Under this hypothesis, the previous rules apply for all of the nucleons. Therefore

$$L_Z = \sum_i l_{Z,i} = \sum_i l_i \tag{1.5}$$

And since the total angular momentum can not be lower than one of its components, then

$$L \simeq \sum_i l_i \tag{1.6}$$

which can be extended to

$$J \simeq \sum_i j_i \tag{1.7}$$

This approach assumes the formation of final nuclei in "stretched" configurations: all the transferred nucleons occupy orbitals coplanar with the scattering plane.

From this analysis, it can be deduced that, for a given experiment, the energy of the beam can be tuned to favor the direct population of the states of interest. Then, the feeding from higher energy states, which would affect the accuracy of the lifetime measurements or even make them impossible in the presence of high-energy isomers, becomes less important.
In addition to this, the analysis done by Zardi shows how the shape of the angular distribution of the residual projectile depends on the reaction dynamics. Therefore, in the case of (^{3}He,n) transfer reactions, by measuring the angular distribution of the emitted neutron it is possible to get information not only about the angular momentum of the populated states in the final nucleus. As an example, Figures 1.1 and 1.2 show neutron angular distributions from the ^{54}Fe(^{3}He,n)^{56}Ni two-proton transfer reaction [8], as a function of the polar angle in the laboratory reference frame and for different values of excitation energy and angular momentum of the states populated in the reaction. The first figure shows how, for the same value of angular momentum of the states populated in the final nucleus, but different excitation energies , the shape of the distribution remains the same, and only the height changes. On the other hand, the second one shows how the shape of the distribution changes with different values of transferred angular momentum.

All of the considerations on transfer reactions done up to now were assuming direct kinematics, where the reaction consists in one or more nucleons being transferred from a lighter projectile to a heavier target. In the past, direct kinematics was the main way nuclear experiments where performed, given the limited capability of accelerators, which could more easily work with light nuclei, and it is how (^{3}He,n) two-proton transfer reactions were performed [8].
However, the same properties of transfer reactions described above hold true if the reaction is performed in inverse kinematics, with nucleons being transferred from lighter targets to heavier projectiles. Given the capabilities of present-day accelerators, such reactions are easily performed, and the they become crucial especially when working with RIBs. In order to move as far as possible from the valley of stability, reactions with unstable nuclei are needed: while these nuclei live long enough to be accelerated after being produced, they can not be used to produce targets. Consequently, performing these reactions in inverse kinematics, where the light nuclei form the target, becomes a necessity.

By comparison, one could think of choosing different beams and targets and perform fusion evaporation reactions to study the same low-lying states in the nuclei of interest. These reactions, however, leave the final nuclei in highly excited states, and the resulting feeding of the low-lying states is detrimental for lifetime measurements. Moreover, the cross section for the production of these highly exotic nuclei in fusion evaporation reactions is very low (typically around 10 μb), compared the value for transfer reactions (which ranges from 1 mb to 10 mb).

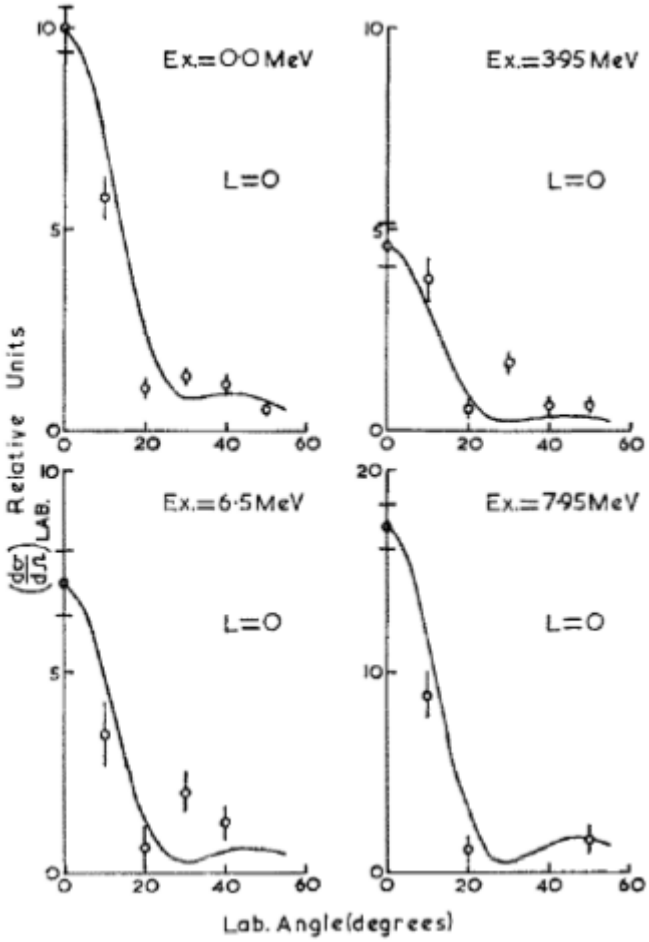

Figure 1.1: Example of neutron angular distributions from the ^{54}Fe(^{3}He,n)^{56}Ni reaction [8], done for the transfer of the same angular momentum (L=0) at different excitation energies. Curves represent DWBA predictions.

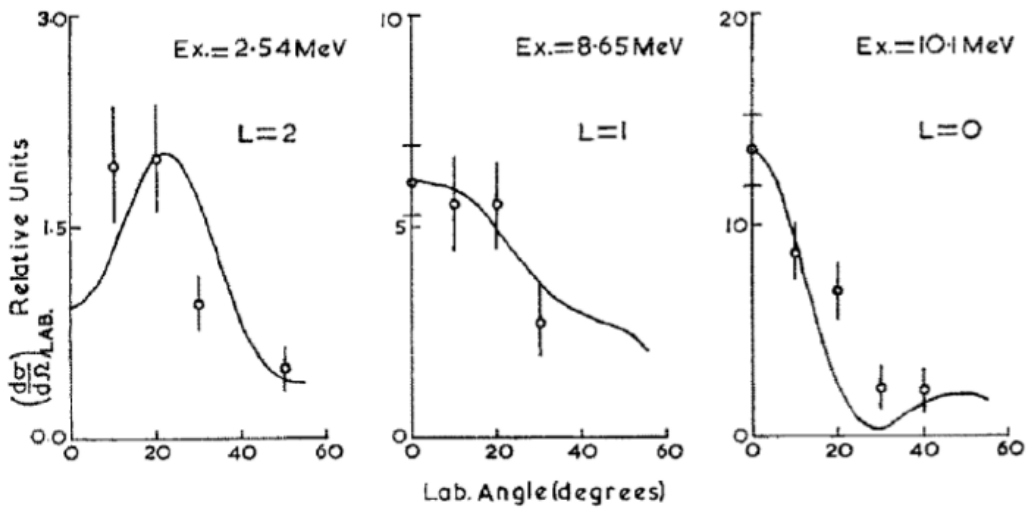

Figure 1.2: Example of neutron angular distributions from the ^{54}Fe(^{3}He,n)^{56}Ni reaction [8], done for different values of transferred angular momentum. Curves represent DWBA predictions.

1.2 Angular distribution measurements with Neutron-Wall

As anticipated, the angular distribution of the emitted neutron in the (^{3}He,n) two-proton transfer reaction provides information on the angular momentum of the populated states in the final nucleus. In the case of the test experiment presented in this work, the emitted neutron is detected by Neutron-Wall [4] in coincidence with γ rays emitted in the de-excitation of the populated states in the final nucleus.
In the past, neutron detectors used to measure neutron angular distributions were placed several meters away from the reaction chamber in order to increase the angular resolution (for example the Large-Area Neutron Detector, LAND [9]). This led to low detection efficiency due to the small covered solid angle, but the high yield of nuclei of interest from the reaction compensated this effect. The purpose of the new target, however, is to be employed in reactions with RIBs in order to study nuclei near the proton dripline: due to the low intensity of the beams and the low cross section of the reactions, the yield is much lower. Therefore, Neutron-Wall was placed only 51 cm away from the target, thus increasing the detection efficiency, but reducing the angular resolution.
In principle, in this configuration Neutron-Wall should be capable of measuring angular distributions, since it has detectors placed at five different angles relative to the direction of the beam, even though with poor angular resolution. Despite the low amount of data points, this is enough to determine the angular momentum, as can be seen in Figure 1.2. In its initial design, however, Neutron-Wall was not intended to be used to measure angular distributions, so during the test experiment the feasibility of this measurement was examined.

1.3 Lifetime measurements via the Doppler Shift Attenuation Method

The Doppler Shift Attenuation Method [2] is a technique used to measure lifetimes between 10^{-13} and 10^{-15} s.

A gold (high Z) backing foil is added to the target to act as an energy degrader. This way, nuclei produced in the reaction of the beam with the target are progressively slowed down. These nuclei are produced in an excited state, from which they decay towards their ground state by emitting γ rays. In the nucleus reference frame, the energy E_0 of the γ rays that are emitted is the difference between the energies of the initial and final level, but in the laboratory reference frame, the measured energy E_m also depends on the Doppler shift caused by the velocity of the decaying nucleus. This effect is proportional to $\cos\theta$, where θ is the angle between the direction of emission and the direction of motion of the decaying nucleus. In inverse kinematics reactions, the distribution of the final nuclei is extremely focused in the direction of the beam, so this effect is dominant for detectors placed at 0° and 180°.

If the lifetime of an excited state is of the longer than ~1 ps, nuclei in that state will decay outside the target after being slowed down. The measured full-energy peak will then be affected by a shift in energy, caused by the Doppler effect related to the average velocity of the nuclei.
However, if the lifetime is shorter, the nuclei will decay while they are still being slowed by the degrader. The full-energy peak will then be affected by a Doppler effect which

depends on the velocity distribution of the nuclei as they are slowing down. This leads to broadening and deformation of the full-energy peak.

Given the target composition and density, the slowing-down of the nuclei can be modeled by using the electronic and nuclear stopping powers [2]. From this, the velocity distribution of the recoiling nuclei can be calculated as a function of lifetime by integrating over the target material and averaging over several different reaction points in the target. By including this information in a Monte Carlo simulation, it is possible to compare the simulated γ-ray spectrum with the measured one and obtain the lifetime of the state.

Chapter 2

The ^{3}He target

The new target consists mainly of a solid ^{nat}W target, with the ^{3}He absorbed in the metallic lattice. At the back of the target, a ^{197}Au foil is added as a support structure; moreover, since the purpose of the target is to be used in the study of short-lived states in neutron-deficient nuclei, the Au foil acts as an energy degrader to allow lifetime measurements with the DSAM technique. Figure 2.1 shows both a cross-section schematic and a front picture of the target.

2.1 The choice of ^{3}He

If one wants to study nuclei close to the proton dripline produced via transfer reactions that employ RIBs, the most promising choice is to have targets of light nuclei that can transfer more than one proton to the projectile. Among these, ^{3}He is the ideal candidate: it can transfer two protons to the projectile of the reaction, thus providing a big leap away from the valley of stability. Furthermore the remaining neutron, which is emitted from the target, can also be detected: the reaction channels of interest can therefore be identified with ease, and by measuring the angular distribution of these neutrons it is possible to know the angular momentum of the populated states in the final nucleus.
Moreover, with ^{3}He as a target the reaction can be performed at energies above the

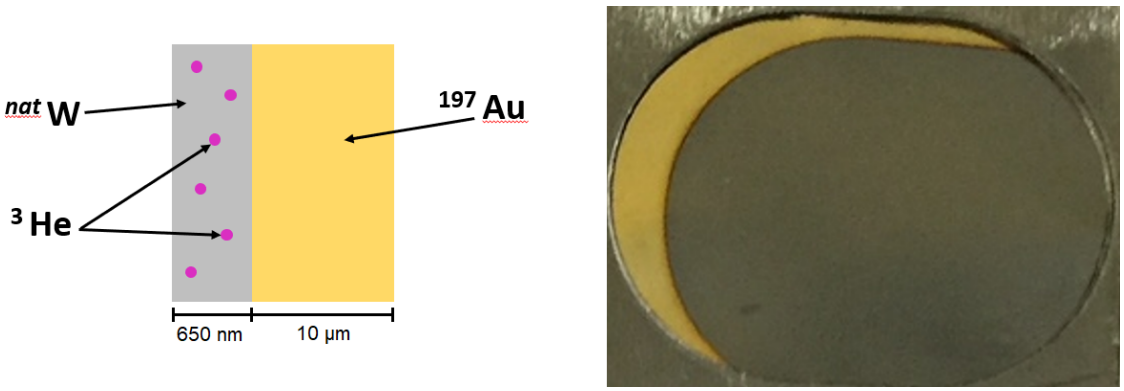

Figure 2.1: Cross-section schematic (left), not to scale, and front picture (right) of the ^{3}He target tested in the experiment. In the picture, the Au backing foil can be clearly seen.

Coulomb barrier, without having to worry about feeding from higher states populated in fusion evaporation reactions, as the evaporation of just one neutron is extremely unlikely.

In principle ^{4}He, which has similar characteristics, could also be used. In this case, however, for the two-proton transfer reactions there are two emitted neutrons. This reaction channel can be identified by detecting either one or both neutrons, but the result is much worse in both cases. Detecting just one neutron includes events where the other neutron is also transferred to the impacting projectile, thus producing nuclei not as far from stability and increasing the background, while the detection of both neutrons is inefficient and loses the information on the transferred angular momentum. Moreover, ^{4}He is strongly bound, so the Q-value of the reaction is less favorable.

Lastly, ^{6}Li could be used, but it adds complexity to the system, and again gathering information on the angular momentum of the populated states in the final nucleus from the angular distribution of the emitted particles is not easily doable. Therefore, among these light nuclei, ^{3}He is the better option.

2.2 Production of the target

The target was produced with an innovative sputtering technique (to be patented). A block of ^{nat}W is placed in a chamber where a plasma of ^{3}He is created. The tungsten block is eroded by the plasma and the emitted particles are progressively deposited on the Au backing foil. In the deposition process, the tungsten carries the helium with itself, trapping it in the metallic lattice that is formed. Unfortunately in the deposition process some contaminants, mainly ^{1}H, ^{12}C and ^{16}O, are also trapped in the metallic lattice.

It is important to note that this technique was initially developed for Si instead of W, and with it an almost negligible quantity of contaminants is present in the target at the end of the procedure. Unfortunately, the Coulomb barrier for Si is too low and fusion evaporation reactions can occur, thus increasing the amount of unwanted events. This has a negative effect when studying nuclei which are produced in low quantity, such as neutron deficient nuclei produced via transfer reactions. Therefore, W was chosen instead: the Coulomb barrier is higher than for Si and fusion evaporation is not a concern. The main reaction channel in this case is Coulomb excitation, which does not represent a problem as the consequent γ rays are not considered when analyzing only those in coincidence with neutrons. Moreover, work is under way to improve the production technique and reduce the presence of contaminants.

2.3 Target properties

The target obtained with this technique has a thickness of 650 nm for the W part, while the Au foil has a thickness of 20 mg/cm^2 ($\sim$10 μm). The effective thickness of ^{3}He is 1.43 μg/cm^2.

The composition of the target has been analyzed with ion beam analysis (IBA) techniques at the SIAM Platform in Namur, Belgium [10]. The results can be seen in Table 2.1: it is immediately clear how contaminants are present in a significant quantity in the target (27.89%). This has a negative effect during experiments due to the increase in background and non-interesting events, and work is already under way to improve the technique and

increase the concentration of ^{3}He while reducing the presence of contaminants. However, as will be shown later, for the purpose of this test the contaminants proved useful to be able to do further analysis of the collected data.
It is important to note that the density of ^{3}He in the target is higher than previous similar targets: in the past, evaporation of ^{3}He from the target, caused by heating due to the impact of the beam, put an upper limit on its density at $\sim 10^{17}$ at/cm^2. Therefore, one of the main concerns during the test was the evaporation of ^{3}He from the target.

Nucleus	Surface density (10^{15} at/cm^2)	Composition %
^{nat}W	2475	64.64
^{3}He	286	7.47
^{16}O	403	10.53
^{12}C	131	3.42
^{1}H	430	11.23
^{28}Si	25	0.65
Other	78	2.06

Table 2.1: Composition of the ^{3}He target.

One last aspect to consider is the behavior of the target in vacuum. After the manufacturing procedure is complete, the target is left inside the production chamber at 10^{-6} mbar for 12 hours. Moreover, for IBA the target is also placed in vacuum. During all this time, no effect is observed regarding the loss of 3He from the target. Therefore, for the duration of an experiment, no problems related to this phenomenon should arise.

2.4 Comparison to other ^{3}He targets

Several different ^{3}He targets have been used in the past for experiments in nuclear physics, but the techniques used in those cases all have shortcomings that make them non optimal for the proposed usage.

Gaseous ^{3}He targets are the between easiest to produce, since ^{3}He is already gaseous at room temperature. Moreover, by employing cryogenic techniques to cool down the chamber where the gas is contained, the density of ^{3}He nuclei can reach quite high values (effective thickness of up to 10^{18} at/cm^2) [11], and even liquid targets can be produced [12]. These targets however, are several cm thick, while extremely thin targets are required for lifetime measurements. This makes them not usable at all for this purpose.

Then there are solid ^{3}He targets produced by implanting low energy (few keV) ^{3}He ions on metallic foils. The typical density of these targets, however, is really low (10^{14} at/cm^2). Higher density targets (10^{17} at/cm^2) have been produced with a variation of this technique [13], but they can only be used in low energy nuclear experiments, as beams with energies higher than a few MeV cause the evaporation of ^{3}He from the target.
Another problem of this technique is the quantity of material that is used. ^{3}He is an extremely rare isotope on earth, and the demand from industry and research applications is wholly met by the decay of ^{3}H which comes from the refurbishment and dismantlement of nuclear weapons [14]. However, following the signing of the START I Treaty between the USA and the USSR in 1991 and the consequent decrease in nuclear warheads kept

ready for use, the ^{3}He global supply has dwindled. Moreover, demand has increased due to its use in medical diagnostic procedures and in neutron detectors, employed in ports and airports for security purposes. All these elements make ^{3}He very expensive, and implantation techniques require a lot of material in the manufacturing process. On the contrary, the innovative sputtering technique used to produce the target tested in this experiment uses a small quantity of ^{3}He: a single target produced this way costs more than 200 times less than a typical implanted target.

Chapter 3

Experimental setup

As explained in the introduction, the test experiment was performed at the LNL with a beam of ^{64}Zn at an energy of 275 MeV, accelerated by the PIAVE-ALPI accelerator complex [15, 16]. This energy is lower than the Coulomb barrier for both ^{nat}W (323 MeV) and ^{197}Au (336 MeV). This way, the only contribution from the reaction of the beam with those nuclei comes from Coulomb excitation and not from fusion evaporation, and the increase in background and unwanted events is limited.
The experiment ran for 22 hours in total, during which two identical targets were used for 11 hours each. The beam intensity was changed several times during the experiment, ranging from 0.5 pnA up to 8.2 pnA (1 pnA $\simeq 6{\cdot}10^9$ particles/s) to test the integrity of the target.

To study the reaction, the GALILEO [3] γ-ray detector array was used, coupled to the Neutron-Wall [4] neutron detector array and the EUCLIDES [5] light charged particle detector array, both used as ancillary detectors to tag the reaction channels.

3.1 The GALILEO detector array

GALILEO [3] is a γ-ray detector array. At the present time, it consists of 25 High Purity Germanium (HPGe) detectors placed around the target at several angles with respect to the direction of the beam:

- 10 detectors at 90°;
- 5 detectors at 119°;
- 5 detectors at 129°;
- 5 detectors at 152°;

Each detector is surrounded by 8 Bismuth Germanate (BGO) crystals that act as anti-Compton shields. Each BGO crystal is screened from direct view of the source by a thick layer of Pb. A picture of the array can be seen in Figure 3.1.
The acquisition of both HPGe detectors and BGO crystals is based on digital electronics.

Figure 3.1: Front picture of the GALILEO γ ray detector array, which shows the 10 detectors at 90°; the remaining 15 are hidden behind.

3.2 The Neutron-Wall detector array

Neutron-Wall [4] is a neutron detector array. It consists of 45 detectors filled with Bicron BC501A liquid scintillator. Like the GALILEO detectors, these are also placed around the beamline at several angles:

- 10 detectors at 18.5°;
- 5 detectors at 30.3°;
- 5 detectors at 34.9°;
- 20 detectors at 47.0°;
- 5 detectors at 57.2°

A schematic and a picture of Neutron-Wall can be seen in Figure 3.2. The acquisition is based on analog electronics.

Neutron-Wall was employed as an ancillary detector for GALILEO to tag neutrons in coincidence with γ rays and highlight the reaction of interest of this work.

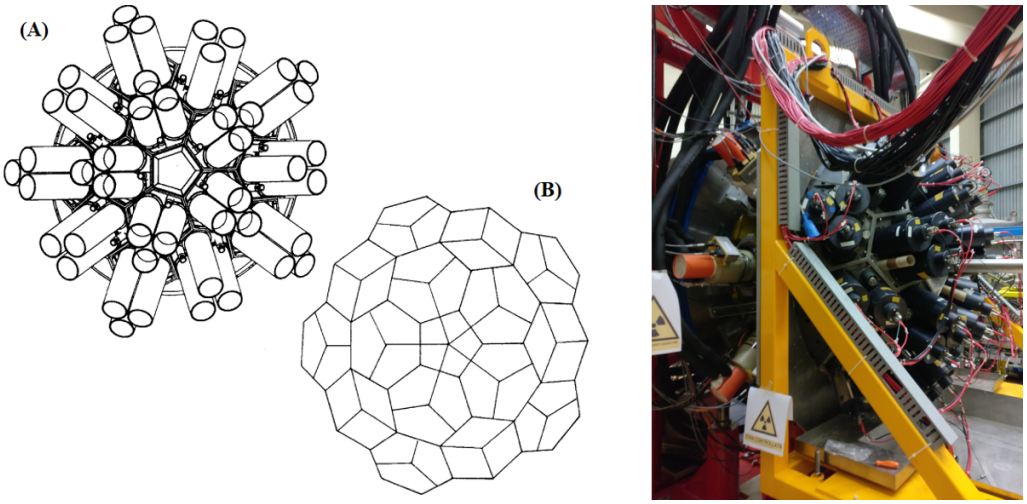

Figure 3.2: The left and center pictures show a schematic of the Neutron-Wall array. (A) shows the back of the array, where the photomultiplier tubes of each detector can be seen. (B) shows the front of the array: the detectors are clustered in groups of three, each cluster covering an hexagonal surface. The picture on the right shows a rear view of Neutron-Wall in the experimental hall; part of the GALILEO detectors at 90° can also be seen on the left side.

3.3 The EUCLIDES detector array

EUCLIDES is a light charged particle detector array [5]. It consists of 55 Si ΔE–E telescopes, placed in a 4π configuration around the target inside the reaction chamber. Each telescope comprises two separate layers of Si, a first one 0.1 mm thick acting as a ΔE detector, and a second one 1 mm thick acting as a total E detector. A picture of EUCLIDES can be seen in Figure 3.3; the whole detector is ∼20 cm in diameter. The acquisition is based on digital electronics.

EUCLIDES was employed as an ancillary detector for GALILEO, together with Neutron-Wall. In the analysis of this experiment, data collected with it was used in different occasions as a veto on γ rays in coincidence with light charged particles, but also to tag reactions where these particles were emitted.

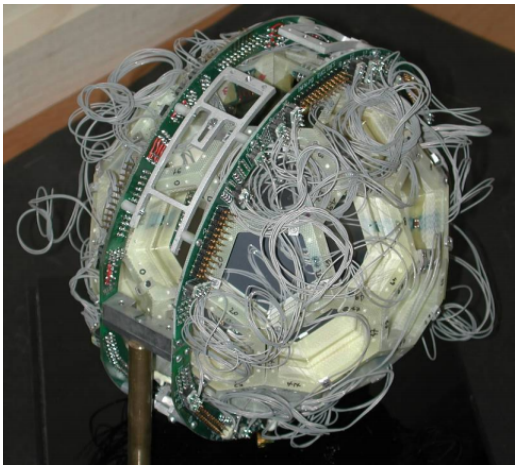

Figure 3.3: Picture of the EUCLIDES detector array.

Chapter 4

Data pre-sorting

Before starting with the analysis of the collected data, several steps are needed to calibrate the detectors, determine their efficiency and provide a way to remove background. This has to be done for each one of the three detector arrays. Moreover, all of them need to be time aligned, so that correlations between γ rays and other detected particles can be better defined by reducing the background and improving the coincidence peak.

4.1 Time alignment

The first thing to do is to align the time of all three detector arrays: they are used to detect particles in coincidence with each other, so this is a fundamental step to properly define the coincidence windows. Each one of the detector arrays is already synced to the others, but single detectors might be off. Therefore, the time of these detectors is aligned with the timestamp of the other ones.

As an example of how this procedure works, Figure 4.1 shows a before/after comparison for the detectors of the GALILEO array. As can be seen in the chart at the top, before the alignment several detectors count the time of the events with an offset when compared to detector 0. In the data pre-sorting, this offset is manually corrected so that all of the detectors count the time the same way and coincidence windows can be easily defined for the whole array.

4.2 GALILEO

For the GALILEO array, an energy calibration needs to be done, and the detection efficiency and the resolution need to be measured. Moreover, Compton suppression and pile-up rejection need to be performed in order to remove part of the background and obtain a cleaner spectrum.

4.2.1 Energy calibration

When a photon interacts with the Ge crystal of one of the detectors of GALILEO, an electric signal proportional to the energy deposited in the interaction is produced and

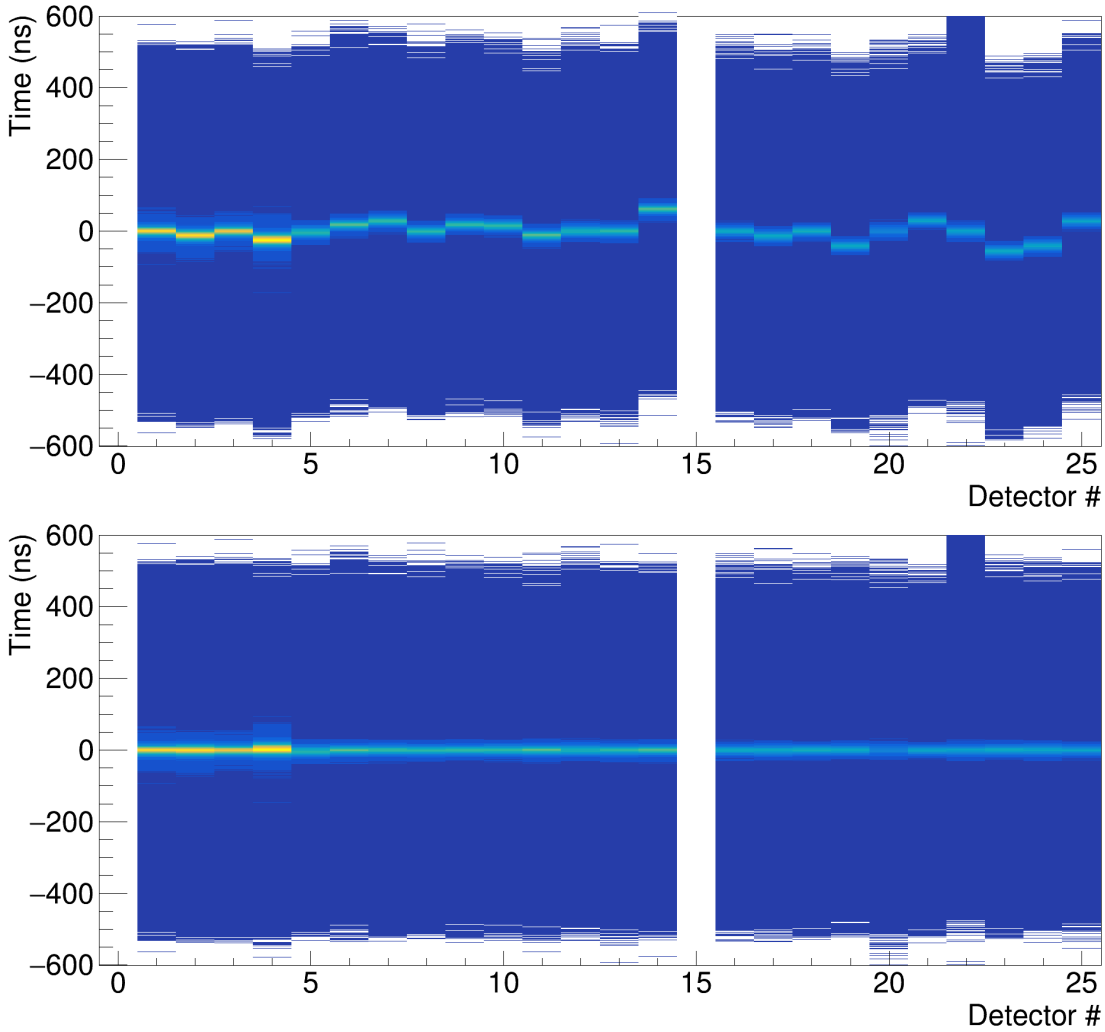

Figure 4.1: Time alignment of each one of the GALILEO detectors, relative to detector 0; the top chart shows the situation before time alignment is performed, while the bottom chart shows the situation after that. In both charts, the central area of each column, which shows a brighter color relative to the background, represents the time difference between the moment photons reach detector 0 and the moment they reach every other detector. Note that columns 0 and 15 are missing: the former would be redundant, as is would show the time difference between detector 0 and itself; the latter is missing because the 25 GALILEO detectors are numbered 16-25 for those at 90°, 0-14 for the rest.

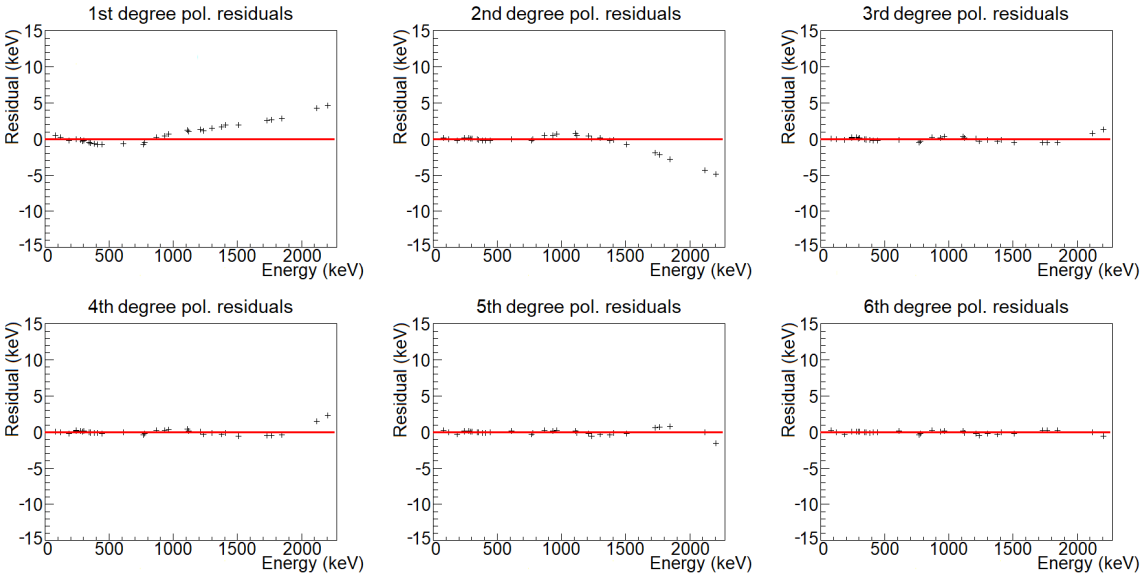

Figure 4.2: Comparison of the residuals from the calibration of one of the GALILEO detectors. The calibration was done with sources of ^{133}Ba, ^{152}Eu and ^{226}Ra.

converted into a digital signal that is analyzed. In order to associate the amplitude of the signal to the deposited energy, each one of the 25 HPGe detectors needs to be calibrated. This was done before the experiment by using radioactive sources that emit electromagnetic radiation of known energy. In particular, sources of ^{133}Ba, ^{152}Eu and ^{226}Ra were used, which provide γ rays ranging between 121 keV and 2204 keV.

Once the measurement is made, the energy of each peak corresponding to the γ decay of an excited state in the source is expressed in "channels". After associating the known energy values to these ones, an energy-channel relation is found via regression methods. Ideally, the relationship between the two would be linear, but small non-linear effects in the electronics chain that processes the signal make this assumption not accurate enough. Therefore, a polynomial relation is used. Of course, higher degree polynomials follow the data points better, but given the strong energy dependence there is the risk that the calibration will be completely off when moving out of the energy range covered by the calibration sources.

In a typical GALILEO experiment, a 5th degree polynomial is used for the calibration. For this particular experiment, however, the detectors were calibrated with a 6th degree polynomial. The choice was made for every single detector based on the analysis of the residuals, shown in Figure 4.2 for one of the GALILEO detectors. As anticipated, 1st degree and even 2nd degree are not very accurate. The other polynomials are all very similar, but the 6th degree one is slightly better at very high energy. Since all of the γ rays from the actual test experiment were expected inside the energy range of the calibration, using such a high degree does not represent a problem.

4.2.2 Efficiency

When analyzing data collected with a γ-ray detector, it is important to keep in mind that the detection efficiency varies with energy. Therefore, the full-energy peak efficiency of the GALILEO array as a function of the energy was calculated from the peaks relative

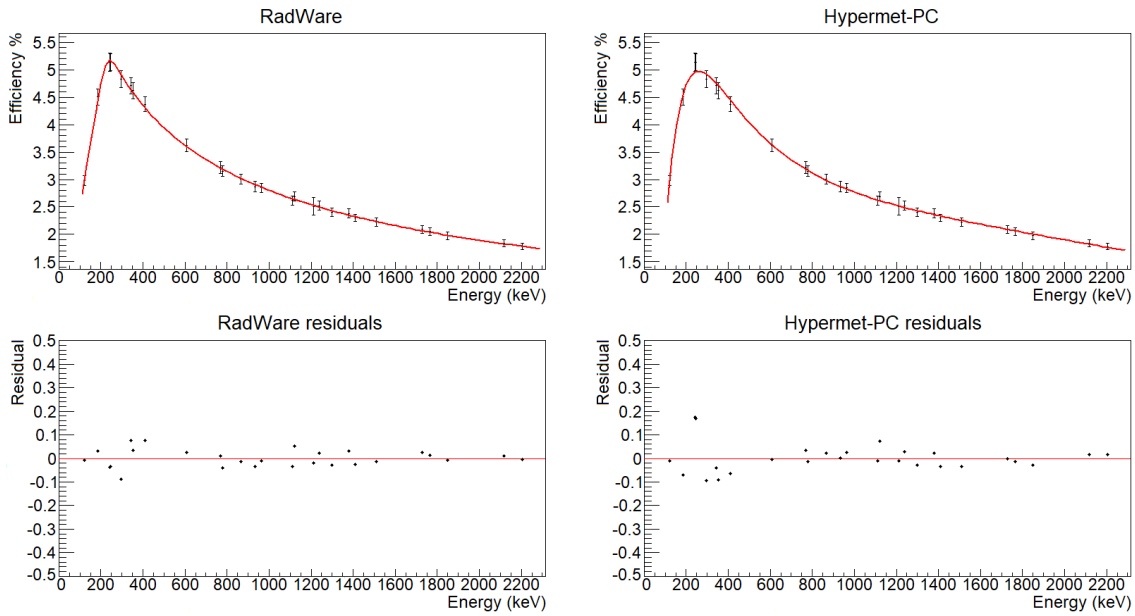

Figure 4.3: Comparison between different efficiency curves for the GALILEO array. The red lines in the top graphs represent the two functions used to fit the data points, RadWare and Hypermet-PC. The two bottom graph show the residuals of each fit. For the efficiency measurements, sources of ^{152}Eu and ^{226}Ra were used.

to the decay of ^{152}Eu and ^{226}Ra. Since the activity of the sources used was known, this allowed the calculation of the absolute efficiency of the array.

In order to correct for efficiency the number of counts at every energy during the experiment, the data points described above were fit with a function. Several functions have been proposed over the years to fit the full-energy peak efficiency of Ge detectors [17]. For the purpose of this work, the functions included in the Hypermet-PC code [18] and the RadWare code [19] were tested to find the best one to use.

The function in the Hypermet-PC code is a high degree polynomial function in the log-log scale, and is supposed to be valid in the 50 keV – 11000 keV range. The expression is:

$$\ln \varepsilon = \sum_{i=1}^{9} a_i (\ln E)^{i-1} \tag{4.1}$$

where ε is the efficiency, E is the energy and a_i are the parameters of the fit.

The function in the RadWare code, instead, includes two different contributions from low energy and high energy, and should be valid at every energy. The expression is:

$$\varepsilon = \exp\left\{\left[\left(a + bx + cx^2\right)^{-g} + \left(d + ey + fy^2\right)^{-g}\right]^{-1/g}\right\} \tag{4.2}$$

where $x = \ln \frac{E}{100\ \mathrm{keV}}$, $y = \ln \frac{E}{1000\ \mathrm{keV}}$, and $\{a, ..., g\}$, are the parameters of the fit.

The results of the two fits are shown in Figure 4.3. Both functions follow the data points quite well: for the RadWare function, the chi-squared test gives $\chi^2 = 0.01$ with 20 degrees of freedom (DoF), while for the Hypermet-PC one it gives $\chi^2 = 0.02$ with 18 degrees of freedom. While the RadWare function is just slightly better than the Hypermet-PC one around the peak of the curve, there is almost no difference at energies above 300 keV,

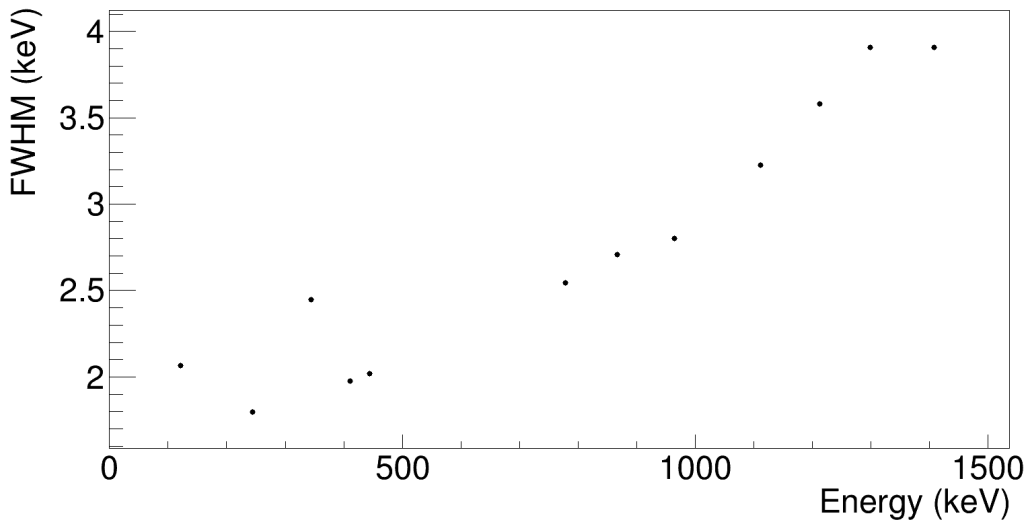

Figure 4.4: Measured resolution of the GALILEO array as a function of the energy.

which is the energy range of interest: if only those data points are considered the test gives $\chi^2_{RadWare} = 0.008$, $\mathrm{DoF}_{RadWare} = 15$ and $\chi^2_{Hypermet-PC} = 0.006$, $\mathrm{DoF}_{Hypermet-PC} = 13$. Since the difference between the two is negligible, for the following analysis the Hypermet function was chosen due to its easier implementation.

4.2.3 Resolution

By analyzing the full-energy peaks relative to the decay of ^{152}Eu, the resolution of the array was estimated. In order to do so, the full-energy peaks in the γ spectrum were fit with a Gaussian curve and the Full Width at Half-Maximum (FWHM) was calculated from the standard deviation (FWHM $= 2\sqrt{2\ln 2}\cdot\sigma$). The results are shown in Figure 4.4. The FWHM at 1 MeV is ∼2.8 keV.

4.2.4 Compton suppression

When a γ ray interacts with a Ge crystal, it might not release all of its energy in a single event: if Compton scattering takes place, only part of the energy is deposited, and the photon is deviated in a new direction, ready to start a new process or to leave the detector without further interactions. Since the signal produced by the detector depends on the deposited energy, if the photon then exits the crystal before releasing all of its remaining energy, the interaction event will be recorded as a lower energy one and will increase the background.

The eight BGO crystals surrounding each Ge detector have high detection efficiency and are used to detect γ rays exiting the Ge crystals. In order to remove the background from Compton scattering, events in each Ge crystal are compared to events in the corresponding BGO crystals: for events in coincidence, the energy deposited in each of the crystals is analyzed. Ideally, only the events where there is no energy deposited in the BGO crystals are good events. In practice, a really low threshold for the energy deposited in the BGO crystals is placed, and events with higher energy are all rejected. This is done to

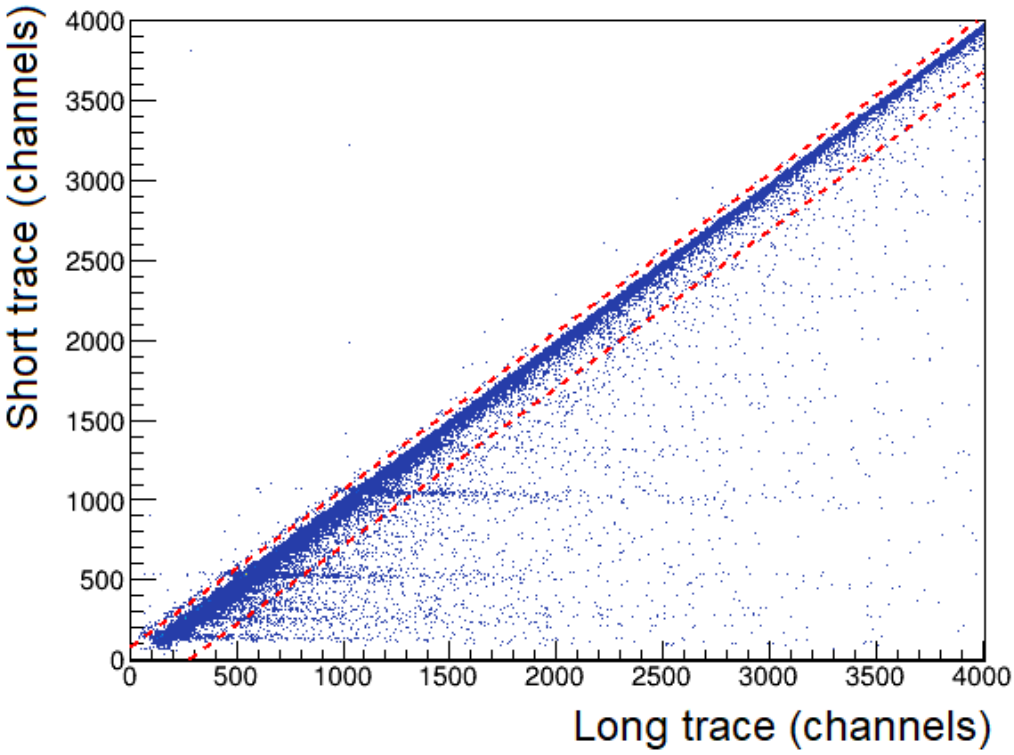

Figure 4.5: Example of pile-up rejection. The short trace of the signal is plotted as a function of the long trace. Then, the dashed lines are traced to determine which events are taken into account; all of the other events are discarded. This plot comes from a previous experiment [20] performed with the same setup as the test experiment presented in this work

compromise between completely removing the background from Compton scattering and keeping high enough statistics in the full-energy peaks.

This operation, as well as the pile-up rejection explained in the next section, is done directly with data from the experiment, as these two phenomena are strongly dependent on the energy of the incoming γ rays and on their production rate.

4.2.5 Pile-up rejection

Sometimes, it can happen that while the signal produced by one γ ray is being collected by the crystal, another γ ray interacts with the same crystal. In this case the event would be registered as a single γ ray of higher energy. Thanks to the digital acquisition of GALILEO, however, the whole shape of the electric signal produced is recorded, so Pulse Shape Analysis (PSA) is possible.

The pulse shape of a single photon is that of an initial peak followed by a long tail. If pile-up happens, a second peak appears over the tail of the first one. In the analysis, the integral of the first part of the pulse, over the peak (short trace) is compared to the integral of the whole signal (long trace). In the case of pile-up, the latter will be much higher than the former: this allows the rejection of pile-up events.

For this experiment, pile-up rejection was performed directly as data was being collected, so in the pre-sorting only some adjustments were required. However, a clear example taken from a previous experiment [20] performed with the same setup can be seen in Figure 4.5:

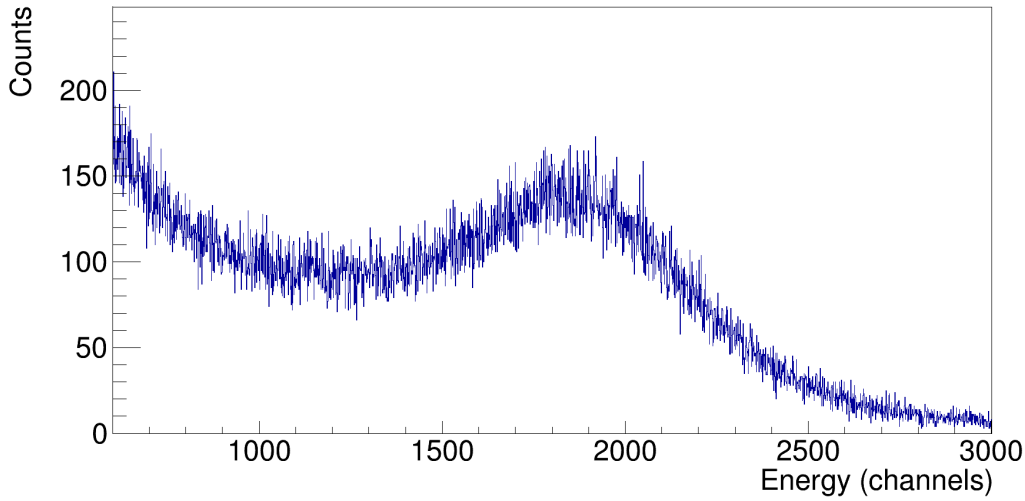

Figure 4.6: Energy spectrum measured by one of the Neutron-Wall detectors when exposed to a source of ^{60}Co, zoomed in on the region where the Compton edge is located.

events where pile-up occurs have a long trace much higher than the short trace; in the plot, these are all of the data points below the thick line at the center. In order to reject these events, data points at the bulk of this line, which includes events where the short trace is roughly the same as the long trace, are fit with a 1st degree polynomial, and an acceptance band is defined around this fit (the band is represented by the dashed lines in the plot). The end result is that all of the events in the thick line are considered, while all of the others are rejected.

4.3 Neutron-Wall

For the Neutron-Wall array, like for the GALILEO array, an energy calibration was done and the relative efficiency of the detectors was measured. Moreover, since the array can detect both neutrons and γ rays, a method of distinguishing between the two must be devised.

4.3.1 Energy calibration

Much like the GALILEO array, the Neutron-Wall array needs to be calibrated in energy. One thing to note is that the energy calibration of Neutron-Wall is not as important as the one of GALILEO, since the energy deposited by neutrons in the detector is not necessarily proportional to their total energy.

For the calibration itself, monochromatic sources of neutrons are not easily available, but Neutron-Wall does also detect γ rays, so γ-ray sources of ^{22}Na, ^{60}Co and ^{137}Cs were used. In this case, however, the channel-energy relation is not found by identifying the full-energy peaks, as almost all of the photons interact via Compton scattering with the detectors, thus releasing only part of their energy. The energy released in Compton scattering by a photon reaches its maximum value when the photon is backscattered: if E is the initial

energy of the photon, the final energy E' is

$$E' = \frac{E}{1 + \frac{E}{m_e c^2}(1 - \cos\theta)} \tag{4.3}$$

where m_e is the mass of the electron and c is the speed of light. The energy released is maximum when the final energy of the photon is minimum, so for $\theta = \pi$. From this, one would expect a well defined Compton edge in the energy spectrum measured by the detector, followed by a region where no data points appear. In the real case, the resolution of the detector comes into play, causing deformation of the edge and the appearance of a very broad peak. An example of this can be seen in Figure 4.6, where the energy spectrum measured by one of the Neutron-Wall detectors with a source of ^{60}Co is shown.

Monte Carlo simulations show how, in these conditions, the position of the real Compton edge is located at higher energy than the peak, where the counts are approximately 90% of the counts of the peak. Therefore, for the energy calibration of each Neutron-Wall detector, the position of the Compton edge for each calibration source was measured following this criterion and compared to the real value:

- ^{22}Na $\rightarrow$ 1061.7 keV;
- ^{60}Co $\rightarrow$ 1040.8 keV;
- ^{137}Cs $\rightarrow$ 477.4 keV.

Since only three data points were available, a linear channel-energy relation was calculated with regression methods, and higher polynomials were not considered.

4.3.2 Neutron and γ rays discrimination

As anticipated, Neutron-Wall can detect both neutrons and γ rays. In order to properly tag the reaction channel of interest, discrimination between the two particles is needed. This is done by analyzing the Time-of-Flight (TOF) of the particles as a function of the Zero-Crossover (ZCO). Let us give a few definitions and description before returning to the main point.

Zero-Crossover The shape of the pulse produced by the interaction of a particle with a Neutron-Wall detector depends on whether the particle is a neutron or a photon. In particular, while the initial rise of the signal is the same for neutrons and γ rays, the decreasing (and slow) part of it is different. Based on this, a Zero-Crossover algorithm can distinguish between γ rays and neutrons [21].

Time-of-Flight During the experiment, the "start" for the measurement of the Time of Flight of the particles is given by a γ ray detected by Neutron-Wall itself, while the "stop" is given by the arrival of a second particle. The Neutron-Wall detectors are placed around the reaction chamber, at a distance of 51 cm from the target: γ rays, which are emitted almost immediately after a reaction, take about 1.7 ns to reach them, while neutrons are slower (of the order of 10 ns).

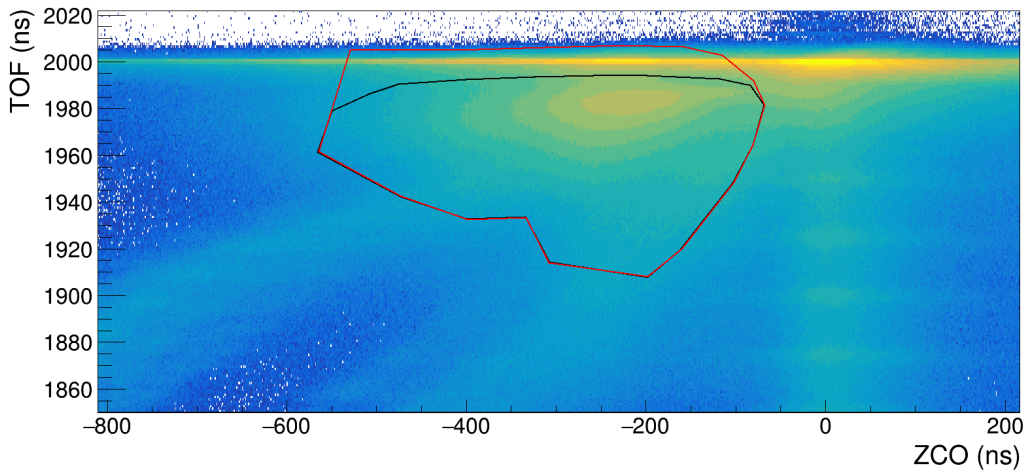

Figure 4.7: Neutron-Wall: TOF as a function of ZCO. Note that for both of them the axes are inverted, so neutrons appear in lower left part, while γ rays are concentrated around ZCO = 0 ns and TOF = 2000 ns (there is an offset of 2000 ns)

Discrimination Either one of the two quantities described above can be used on its own to distinguish between neutrons and γ rays, but if they are used together they provide better discrimination. Therefore, both of them are used at the same time, as seen in Figure 4.7. In particular, two cuts are used for neutron identification: a small cut (black) only selects the region where TOF and ZCO correspond to those of neutrons; a second, larger cut (red) selects instead a region where the ZCO is still the one of neutrons, but TOF including γ rays is also taken into account. This is because in the transfer reaction of interest, neutrons are expected to be emitted with energies up to more than 20 MeV: given the time resolution of the Neutron-Wall detectors ($\sim$2 ns), the TOF of these fast neutrons is not really distinguishable from the one of photons, and a larger cut is needed.

4.3.3 Efficiency

One of the goals of this experiment was to test the feasibility of neutron angular distribution measurements with Neutron-Wall. In order to get the correct trend of the distributions, the relative efficiency of the detectors is needed. A source of ^{252}Cf was used for this measurement, as it emits neutrons isotropically with a very broad energy distribution peaked at $\sim$1 MeV (shown in Figure 4.8). The TOF-ZCO technique was used so that the relative efficiency of detecting only neutrons would be measured.

The results of this measurement are presented in Figure 4.9, which shows how the neutron detection efficiency varies quite a lot for different detectors: the differences, relative to detector 0 taken as reference, reach as high as 20%.

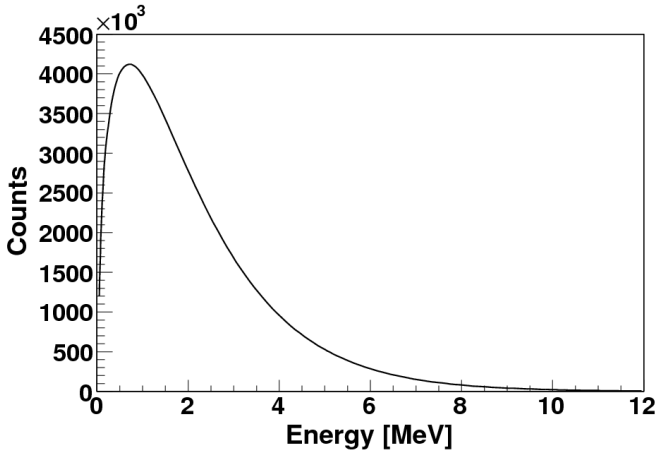

Figure 4.8: Energy distribution of neutrons emitted in the decay of ^{252}Cf.

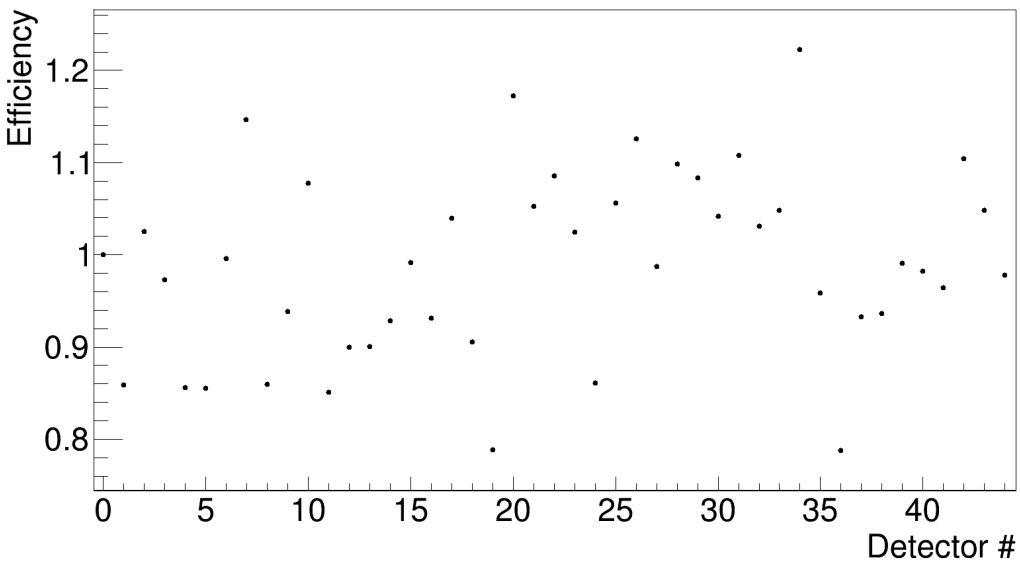

Figure 4.9: Neutron detection efficiency of each Neutron-Wall detector relative to detector 0. The error bars are too small and are covered by the data points themselves. The measurement was done with a source of ^{252}Cf.

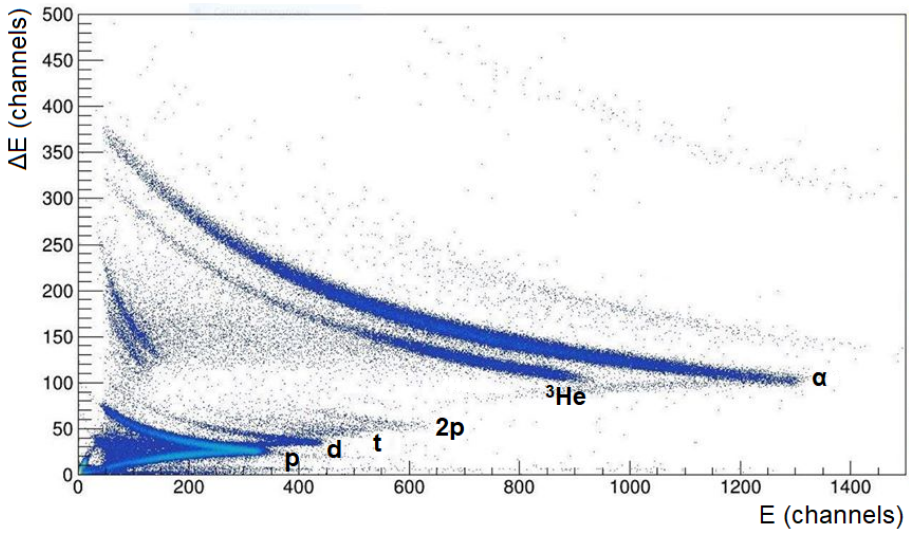

Figure 4.10: ΔE-E matrix for one of the EUCLIDES detectors, with the different detected particles highlighted.

4.4 EUCLIDES

For the EUCLIDES array, the only operation needed is the analysis of the ΔE-E matrices, so that proper particle identification can be done.

When a charged particle travels through a medium, it interacts via Coulomb interaction and progressively transfers its energy to the medium. For a particle of charge z, mass m and velocity v, the loss of energy is given by the Bethe formula, which gives

$$\frac{dE}{dx} \sim \frac{z^2}{v^2} \tag{4.4}$$

while the total energy of the particles is, in a non-relativistic approximation

$$E = \frac{1}{2}mv^2 \tag{4.5}$$

therefore

$$\frac{dE}{dx}\,E \sim mz^2 \tag{4.6}$$

By plotting the ΔE, which is the energy lost in the first layer of the silicon telescopes, as a function of E, reconstructed from the energy lost in both layers, several hyperbolic trends can be seen, each corresponding to different particles. This is how the distinction between protons, deuterons, tritons and alpha particles is done. An example of this can be seen in Figure 4.10. In the pre-sorting of data, in order to select the particles in coincidence with γ rays, cuts much like those made for neutrons are drawn, one for each type of particle. This is done for each one of the 55 detectors.

Chapter 5

^{3}He target test results

In this chapter, the results of the test of the new ^{3}He target are reported. In particular, the analysis focused on the following aspects:

- target damage at the end of the experiment;
- evaporation of ^{3}He from the target;
- yield of the transfer reaction ^{64}Zn(^{3}He,n)^{66}Ge;
- impact of the contaminants present in the target.

5.1 Target damage

The target was visually examined at the end of the experiment to check the amount of damage it had sustained. Figure 5.1 shows a before-and-after comparison of the target. The only significant sign of the impact of the beam is the light gray area that appears near the center; the spots where the tungsten appears to have been removed are due to scratches done when removing the target from the holder inside the reaction chamber.

In the conditions of this test experiment, at these beam energy and intensities, thin targets typically melt or are perforated. The fact that this target showed minimal signs of damage by the end of the experiments tells us that it has high resistance to the impact of the beam.

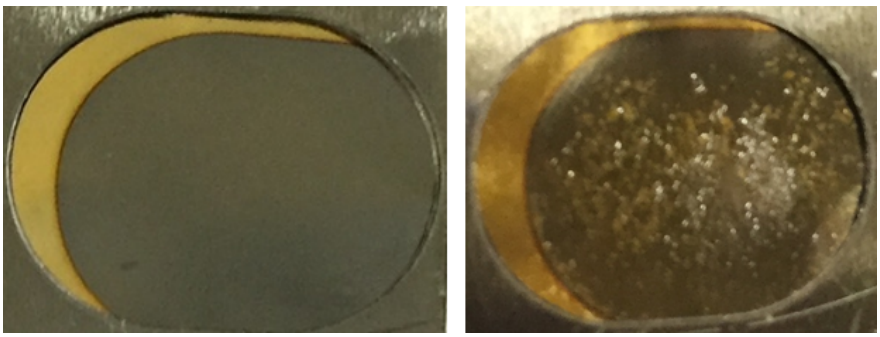

Figure 5.1: Pictures of the target before (left) and after (right) the experiment. The target shows minimal signs of wear.

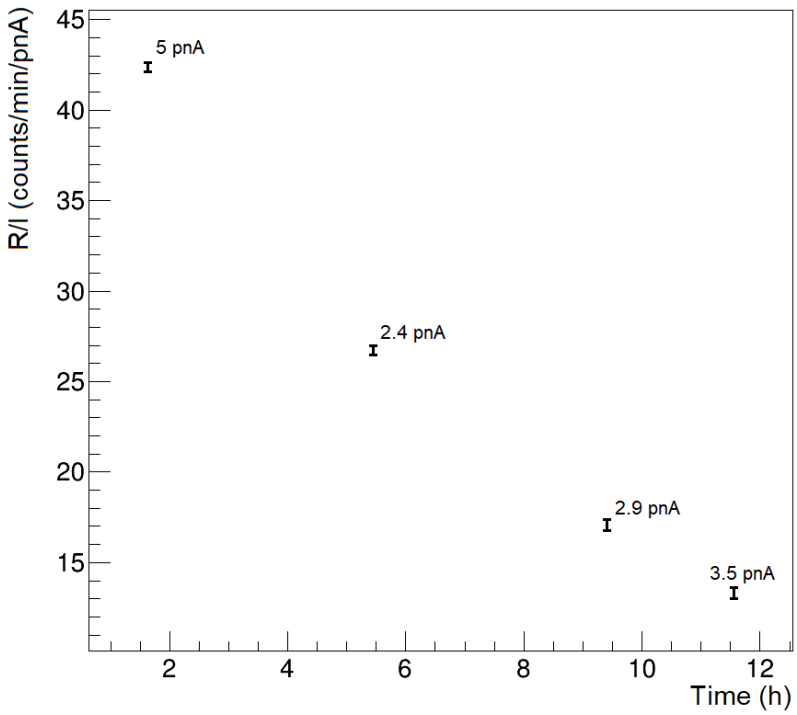

Figure 5.2: Change over time of the counting rate of ^{3}He in one of the front facing detectors of EUCLIDES. The counting rate has been normalized for the intensity of the beam at every moment.

5.2 ^{3}He evaporation

One of the main concerns regarding this kind of target is the resistance to heating. Due to the release of beam energy in the Au and W substrates the target is heated, which can cause the evaporation of ^{3}He. This would decrease the concentration of ^{3}He and have a negative effect on the experiment.

One way to check the relative concentration of ^{3}He is to monitor over time the counting rate of one of the products of the reaction of the beam with ^{3}He. The rate of a reaction is

$$R = I \cdot \sigma \cdot \Delta x \cdot n \tag{5.1}$$

where I is the intensity of the beam, σ is the cross section of the reaction, Δx is the thickness of the target and n is the density of the target nuclei. If the change in target density is caused only by the reaction of the target with the beam, then

$$dn = -\frac{R}{V}dt = -\frac{I\sigma\Delta x}{V} \cdot n \cdot dt \tag{5.2}$$

where V is the volume of the target that the beam goes through. Therefore

$$n = n_0 e^{-\frac{I\sigma\Delta x}{V}t} \tag{5.3}$$

In conclusion, the counting rate is expected to decrease over time following an exponential trend. In practice, the rate of the reaction is typically so low that the impact of this loss can not be observed. Just as an example, for an experiment with beam intensity $I = 10^{10}$ particles/s, beam spot of 4 mm^2, reaction cross section $\sigma = 100$ mb and duration $t = 10$

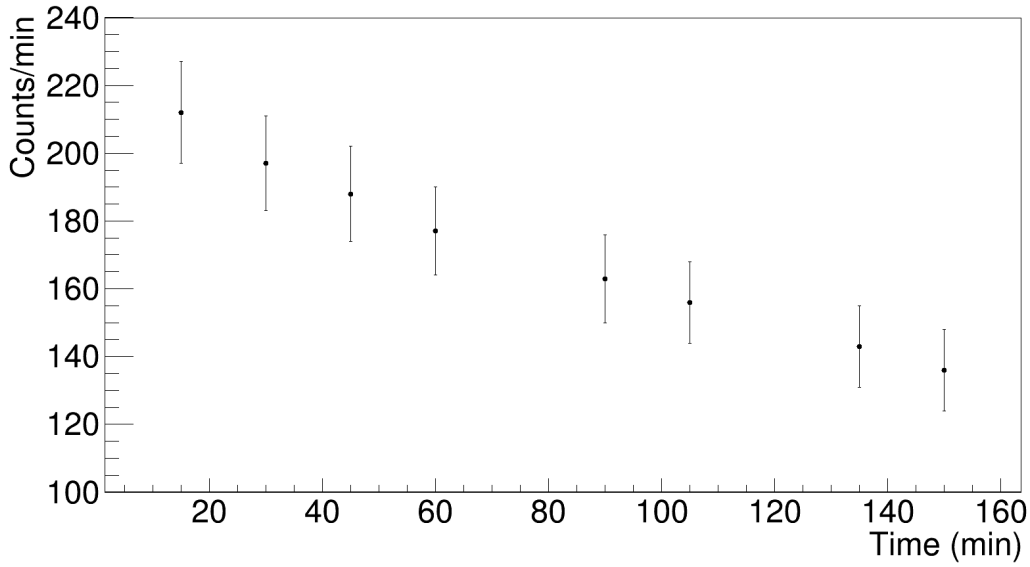

Figure 5.3: Change over time of the counting rate of ^{3}He in one of the front facing detectors of EUCLIDES. For all of the data points in this chart, the intensity of the beam is constant at 5 pnA.

h, the ratio between the final and initial target densities is $\frac{n}{n_0} = 1 - 10^{-9}$.
On the other hand, if evaporation occurs the loss of ^{3}He from the target proceeds faster, and can have an observable effect on the reaction rate. The rate of evaporation is related to the temperature reached by the target, which in turn depends on the intensity and energy of the beam: calculations done with the Cologne code [22] show that with a beam with an energy of 233 MeV and an intensity of 2.4 pnA, the target reaches 78 °C at the beam spot; in the same conditions, but with an intensity of 10 pnA, the target reaches 260 °C at the beam spot.

The first counting rate that one could think of monitoring is the one of γ rays relative to the de-excitation of ^{66}Ge produced in the two-proton transfer reaction ^{64}Zn(^{3}He,n)^{66}Ge. However, as will be shown later, the number of detected γ rays relative to this phenomenon is really low, and a somewhat clean peak in the energy spectrum can only be seen when the sum of all the statistics is observed. Therefore, the counting rate of ^{3}He seen in EUCLIDES was observed instead: due to elastic scattering with the beam, ^{3}He is expelled from the target, mainly in the direction of the beam.

The value of the counting rate of ^{3}He in one of the front facing detectors of EUCLIDES, normalized for the intensity of the beam, is shown in Figure 5.2 for the second target used. With this target, the current was varied between 2.3 and 5 pnA. From the chart, it can be seen how the counting rate decreases significantly over time: the only possible explanation for this is the evaporation of ^{3}He from the target. However, between the start and the end of the experiment, the counting rate decreased only by a factor of $\sim$3.
It is also interesting to see how the counting rate changes over time at constant beam intensity: this is shown in Figure 5.3. Considering that the intensity of the beam was quite high, this is a really positive result: evaporation of ^{3}He from the target does indeed occur, but the effect is moderate. Moreover, when the lower beam intensities of RIBs are taken into account (typically up to 10^6 particles/s) the effect of evaporation should become negligible.

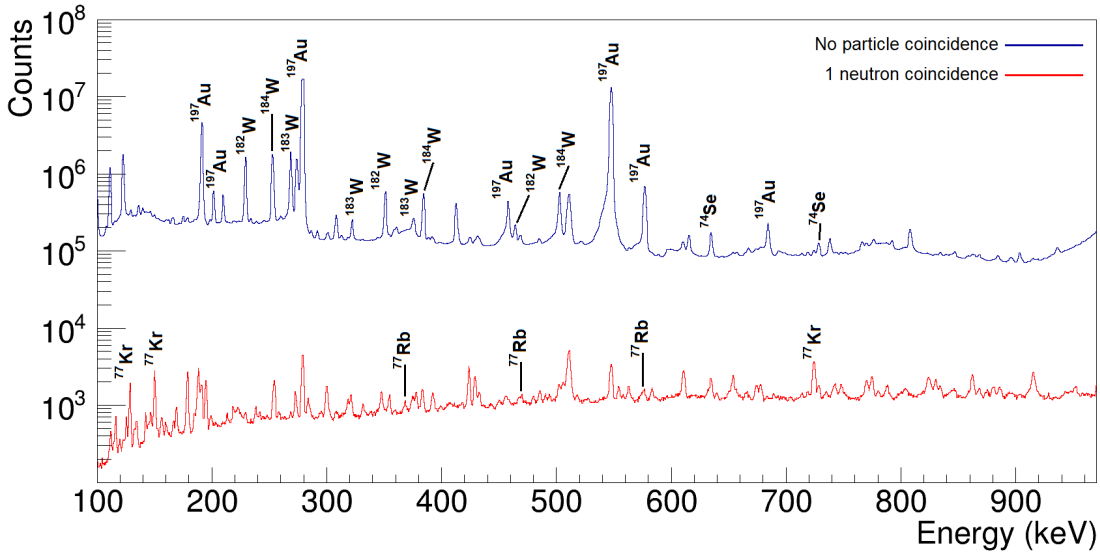

Figure 5.4: Comparison of the γ-ray energy spectrum measured by GALILEO, with (in red) and without (in blue) the condition of coincidence between each γ ray and one neutron. To produce this spectrum, the small neutron cut in the TOF-ZCO matrix shown in Figure 4.7 was used. For some of the peaks, the corresponding nucleus is reported.

5.3 Two-proton transfer reaction

The reaction of interest for which the target was built is the two-proton transfer reaction ^{64}Zn(^{3}He,n)^{66}Ge. Thanks to the selectivity of transfer reactions, only the excited states with low energy, low angular momentum can be populated in ^{66}Ge.

Since in the reaction of interest a single neutron is emitted, in the analysis of the γ-ray energy spectrum only γ rays in coincidence with single neutrons and no charged particles were taken into account. This operation removes all of the γ rays that are not in coincidence with neutrons, provides a clean spectrum and allows the observation of full-energy peaks that might otherwise be submerged by the background or by uninteresting events. The effect of this procedure can be seen in Figure 5.4. The blue line represents the energy spectrum of every γ ray detected, while the red line is the energy spectrum of γ rays in coincidence with one neutron. In the former, many of the peaks come from the de-excitation of ^{197}Au and ^{nat}W, excited by the beam via Coulomb excitation, or from the de-excitation of nuclei produced in fusion evaporation reactions with the contaminants present in the target. On the other hand, in the spectrum obtained in coincidence with one neutron many of those peaks are reduced or even removed, causing the appearance of new peaks that would otherwise not be seen.

The energy spectra in coincidence with neutrons were produced by using both the small and large cuts for neutron-γ discrimination shown in Figure 4.7.
The large one was chosen first in an effort to include both slow and fast neutrons, so that the high-energy neutrons ($E_n > 20$ MeV) emitted in the two proton transfer reaction would also be considered. However, the region where high energy neutrons are located also includes γ rays: as a consequence of this, the background was not removed enough and γ rays coming from the de-excitation of ^{66}Ge could not be seen.
On the other hand, the small cut excluded the high energy neutrons, but also a big part of the γ rays detected by Neutron-Wall. As a result, despite not considering some of the

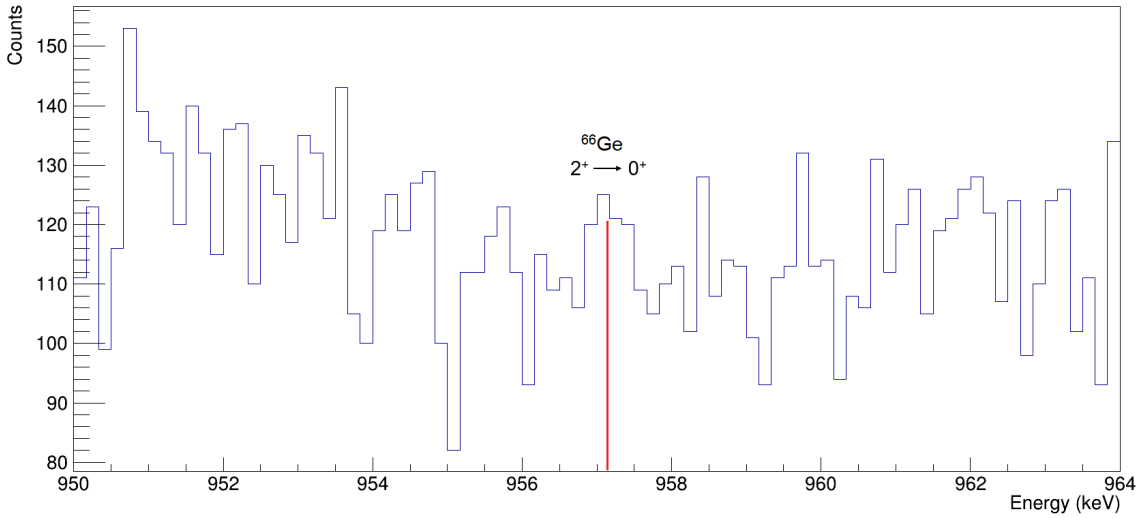

Figure 5.5: Neutron-gated γ-ray energy spectrum, zoomed in on the region of interest, that shows the 957 keV transition of ^{66}Ge.

"good" events, thanks to the reduction of the background it was possible to identify the transition corresponding to the de-excitation of the lowest excited state in ^{66}Ge: it is an E2 transition from the first 2^+ excited state at 957 keV to the 0^+ ground state. The peak in the energy spectrum corresponding to this transition can be observed in Figure 5.5. The position of the peak is found at 957.17 (17) keV, while the reference value reported on the NNDC Database is 956.94 (8) keV [23]. The clean area (after removing the background by estimating its value from the valleys beside the peak) gives 56 (7) counts. Due to the high background, the peak is barely visible, but the following two aspects lead to it being considered as more than a statistical fluctuation:

- un-gated, proton-gated or α particle-gated γ-ray spectra do not show anything noteworthy around 957 keV, only the neutron-gated ones do;

- The background below the peak consists of 433 counts, while the whole peak consists of 489 counts. Considering the Poisson Distribution, with expected value $\lambda = 433$, this gives $P_{433}(n \geq 489) = 0.004$.

From the clean area of the peak, knowing the duration of the experiment, the intensity of the beam, and the properties of the target and of the detectors, it is possible to get a rough estimate of the cross section of the reaction: the result is $\sigma \simeq 0.3$ mb. This value is one order of magnitude lower than the expected one ($\sim$1 mb), but one needs to consider that the peak is barely visible over the background, and also all of the γ rays in coincidence with high-energy neutrons were discarded when employing the small cut in the TOF-ZCO matrix.

After finding the peak, the γ-γ coincidence technique was used look for other γ transitions in ^{66}Ge, such as the $4_1^+ \rightarrow 2_1^+$ (1216 keV) or the $2_2^+ \rightarrow 2_1^+$ (736 keV). Figure 5.6 shows the energy spectrum of γ rays detected in coincidence with one neutron and with the 957 keV γ transition of ^{66}Ge: once the background is removed, no peaks can be observed at the expected energies.

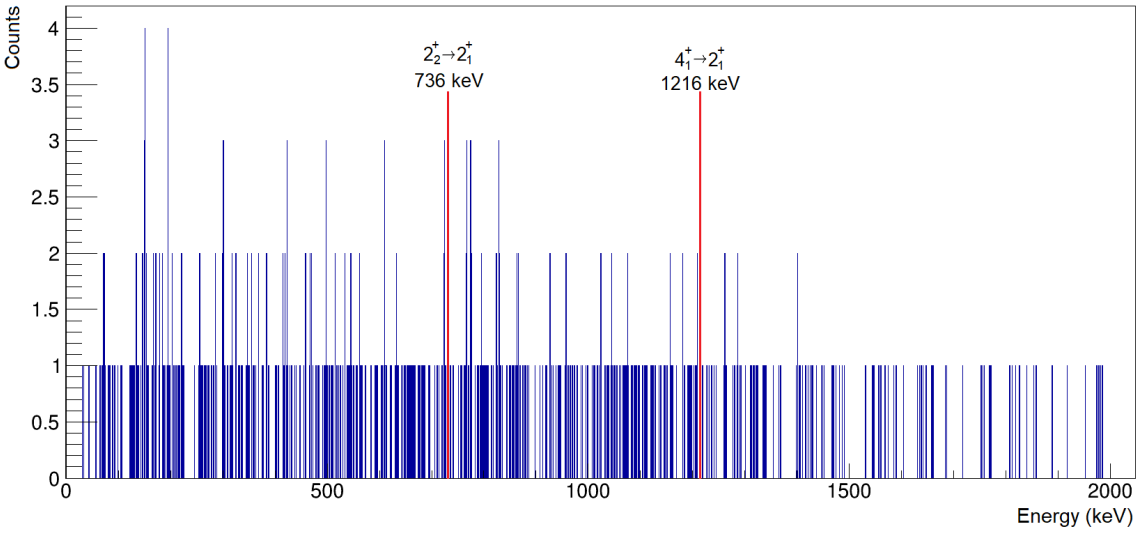

Figure 5.6: γ ray-energy spectrum obtained in coincidence with one neutron detected by Neutron-Wall and with the γ transition at 957 keV of ^{66}Ge. The expected energy of the transitions at 736 keV and 1216 keV are reported.

5.4 Contaminants

The target composition, showed in Table 2.1, reports a high quantity of contaminants. In particular, ^{12}C and ^{16}O are the most problematic ones, as they are some of the most present inside the target. At the typical energies of experiments, fusion evaporation reactions with these nuclei can occur: given the high cross section of these reactions, γ rays emitted by the nuclei produced this way increase the background and can drown out rare events associated to the two-proton transfer reaction.

For this test experiment in particular, in the analysis of the γ-ray energy spectrum peaks corresponding to the de-excitation of ^{74}Se, ^{77}Kr and ^{77}Rb can be observed, all with a much higher number of counts than the peak at 957 keV of ^{66}Ge. All of these proved extremely useful for the following part of the analysis.

Chapter 6

Neutron angular distributions

The second purpose of this test experiment was to examine the feasibility of neutron angular distributions with the Neutron-Wall array.

In the description of the array, it was shown how the detectors are organized in five rings with respect to the beamline. This allows the measurement of the direction of emission of the neutrons. However, Neutron-Wall was not designed with this functionality in mind, and the single detectors are quite large. In particular, the rings have an angular aperture that varies between 8.2° and 11.8°, which means that the angular resolution is not very precise. Nonetheless, angular distribution measurements should still be possible to an extent. For these reasons, the test of feasibility done in this experiment is still of great interest, and this is the first time that such analysis is performed on data collected by Neutron-Wall.

Single neutrons are detected in coincidence with the γ ray transitions of the nuclei of interest. The amount of neutrons counted this way by each detector is then background-subtracted and efficiency-corrected. The counts from detectors belonging to the same ring are summed and then normalized by dividing for the number of detectors in each ring. Lastly, the amount of detected neutrons is plotted as a function of the polar angle θ, which corresponds to the center of each ring of Neutron-Wall. The trend obtained this way is almost the neutron angular distribution: it is lacking a multiplicative factor that accounts for the absolute efficiency of the detectors, which is not known. However, the obtained result is still sufficient, as it can be compared to theoretical calculations or simulations by simply normalizing the measured trend with the predicted one.

6.1 Neutrons from fusion evaporation reactions

As mentioned in the description of the target, a high concentration of contaminants is present. One of them is ^{16}O: the reaction with the beam happens at an energy higher than the Coulomb barrier (49 MeV). This opens up many additional reaction channels, and between these is fusion evaporation. In this reaction, the compound nucleus that is formed is ^{80}Sr: some of the residual nuclei are produced from this via neutron evaporation, such as ^{77}Kr (two protons and one neutron) and ^{77}Rb (one proton and two neutrons).
These two nuclei are between the main products of the fusion evaporation reaction between ^{64}Zn and ^{16}O. The peaks in the γ spectrum corresponding to transitions of these nuclei

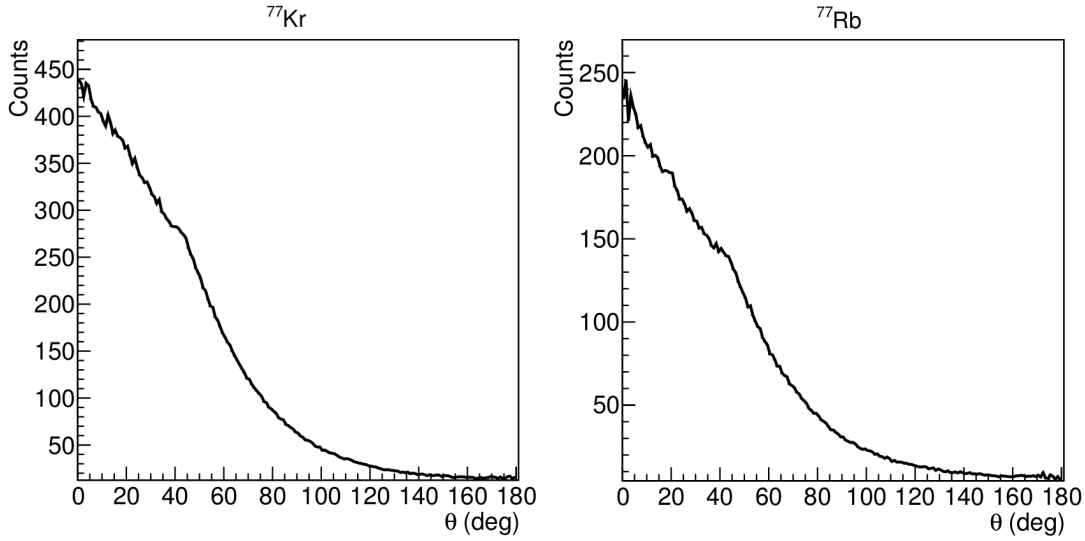

Figure 6.1: Angular distributions of neutrons emitted in the fusion evaporation reactions ^{16}O(^{64}Zn,2p1n)^{77}Kr (left) and^{16}O(^{64}Zn,1p2n)^{77}Rb (right). The distributions were calculated with the fusion evaporation code LILITA_N11 [24].

rise well above the background: this makes them good candidates for the first attempt at measuring neutron angular distributions.

As for the expected distribution, in the intrinsic reference frame of the evaporating nucleus, particles are emitted isotropically: in the laboratory reference frame, the distribution takes into account the kinematic boost given by the velocity of the nucleus. Therefore, the distribution is expected to decrease as the polar angle increases.
In order to compare the measured data, the expected angular distributions were calculated with the fusion evaporation code LILITA_N11 [24]. The results of the calculations are shown in Figure 6.1: both distributions follow the expected trend.

For the measurements, in the case of ^{77}Kr neutrons in coincidence with the γ transition at 724 keV ($13/2^+ \rightarrow 9/2^+$, multipolarity E2) were considered, as it was the most clearly visible one in the one neutron gated spectrum.
On the other hand, for ^{77}Rb the most intense γ transition visible in the one neutron gated spectrum was the one at 470 keV ($9/2^- \rightarrow 5/2^-$, multipolarity E2). The angular distribution of neutrons in coincidence with these γ rays is shown in Figure 6.3.
The results of the two measurements are presented in Figures 6.2 and 6.3 respectively, and the calculated distributions are also plotted. The data points follow the calculate trends in both cases, although they are slightly off in the case of ^{77}Kr.

The result is overall positive, as it shows that Neutron-Wall is indeed capable of measuring neutron angular distributions. Based on this, the next step is the measurement of angular distributions of neutrons emitted in the two-proton transfer reaction ^{64}Zn(^{3}He,n)^{66}Ge.

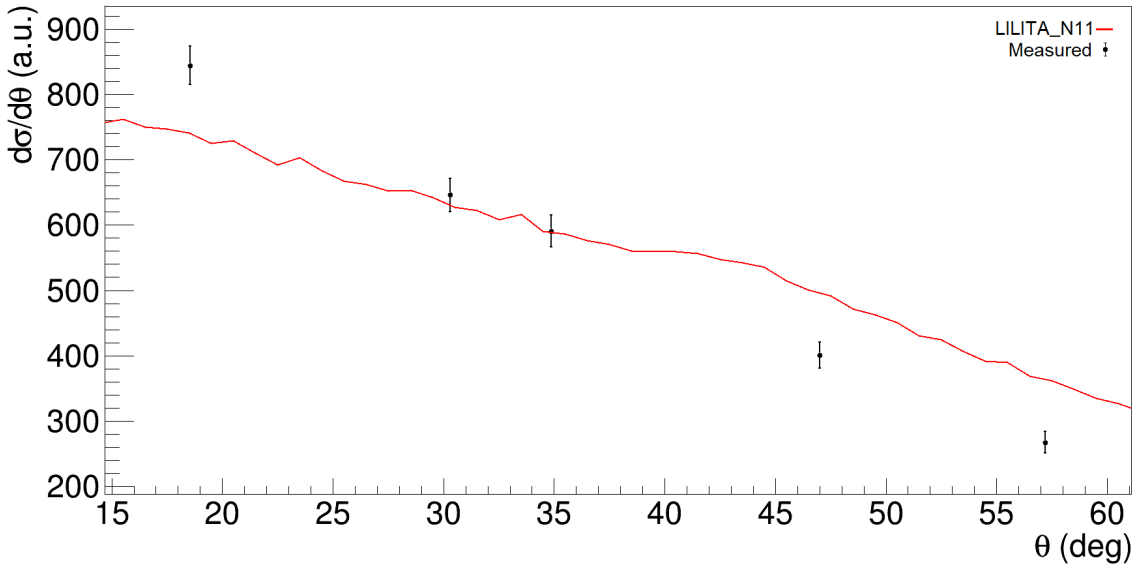

Figure 6.2: Angular distribution of neutrons in coincidence with γ rays from ^{77}Kr at 724 keV. The measured distribution is compared to the one calculated with the LILITA_N11 code and normalized to the measured points.

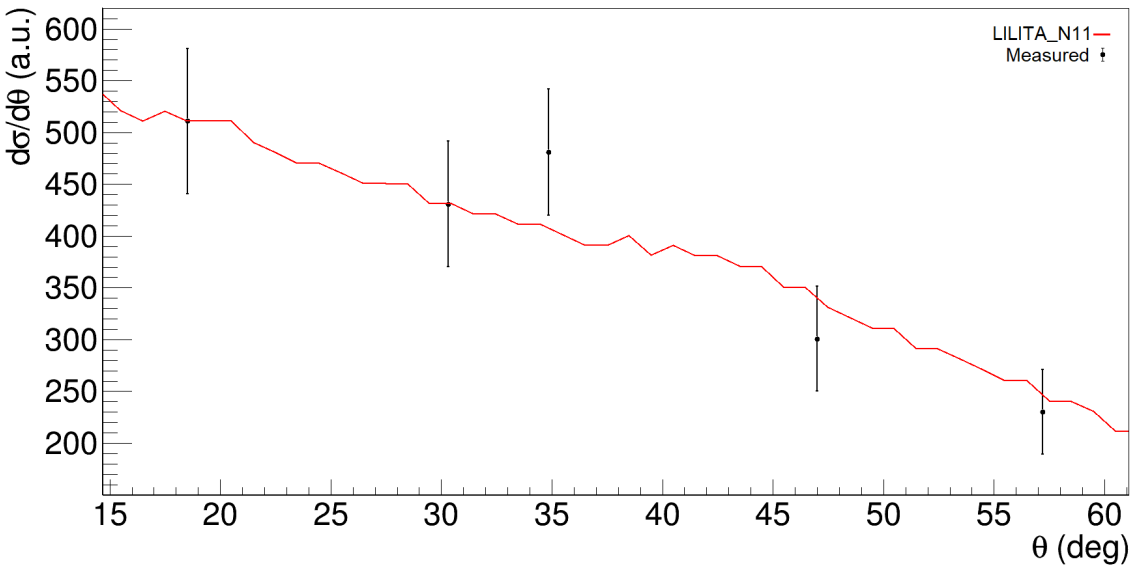

Figure 6.3: Angular distribution of neutrons in coincidence with γ rays from ^{77}Rb at 470 keV. The measured distribution is compared to the one calculated with the LILITA_N11 code and normalized to the measured points.

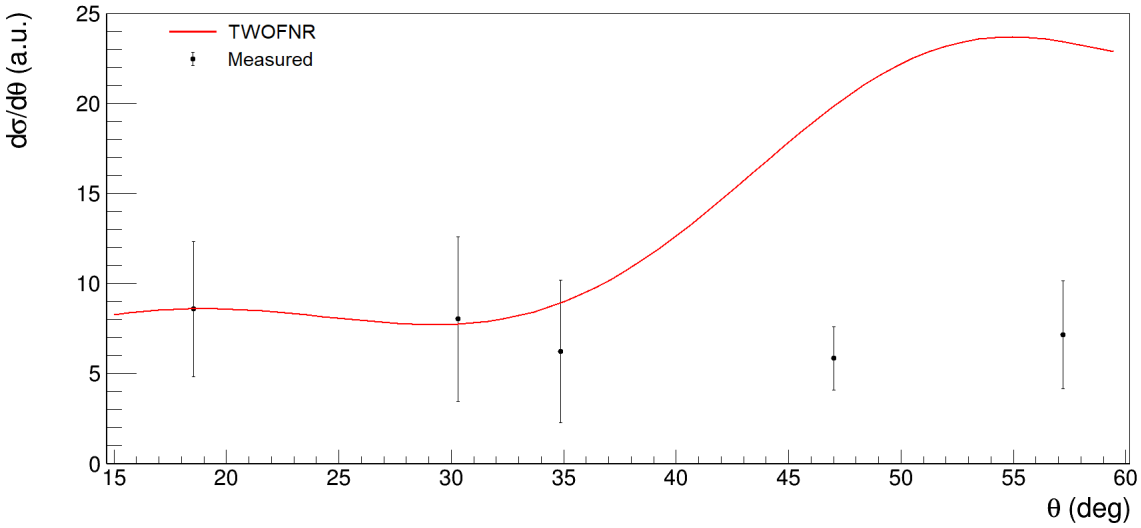

Figure 6.4: Angular distribution of neutrons in coincidence with γ rays from ^{66}Ge at 957 keV. The measured distribution is compared to the one calculated with the TWOFNR code and normalized to the measured points.

6.2 Neutrons from the two-proton transfer reaction

Given the positive result in the measurement of neutron angular distributions in the case of fusion evaporation reactions, the next measurement was done with the neutrons emitted from the two-proton transfer reaction ^{64}Zn(^{3}He,n)^{66}Ge. The aim is to gather information on the angular momentum of the populated state from the angular distribution of the emitted neutrons: Neutron-Wall can provide data points at five different polar angles. Similar measurements done in the past [8] show that this is enough to determine the angular momentum at least for small multipoles, as can be seen in Figure 1.2.

For this measurement, neutrons in coincidence with the γ transition of ^{66}Ge at 957 keV ($2^+ \rightarrow 0^+$) were considered. However, given the low amount of γ rays detected, the number of neutrons was also really low, so much that after removing neutrons from the background 13 of the 45 detector did not have counts at all. As a result of the very low statistics, the errors are quite large ($\sim$30%), which can be seen in Figure 6.4. The same plot also shows a comparison with the normalized angular distribution calculated for the two-proton transfer reaction that populates the 2^+ state. The calculation was done with the TWOFNR code [25], and the full distribution can be seen in Figure 6.5. It is clear that the measured trend differs completely from the calculated one: the statistics of the measured data are too low to provide any good information.

6.3 Angular distribution measurement feasibility: conclusions

Apart from the low angular resolution of the detectors, one of the main concerns regarding this kind of measurement was the impact of neutrons scattering between detectors.

If for example a neutron interacts initially with one detector and in the collision is deviated towards another detector with which it interacts again, two signals are collected. Due to the time resolution of Neutron-Wall, it is not possible to tell which interaction takes place

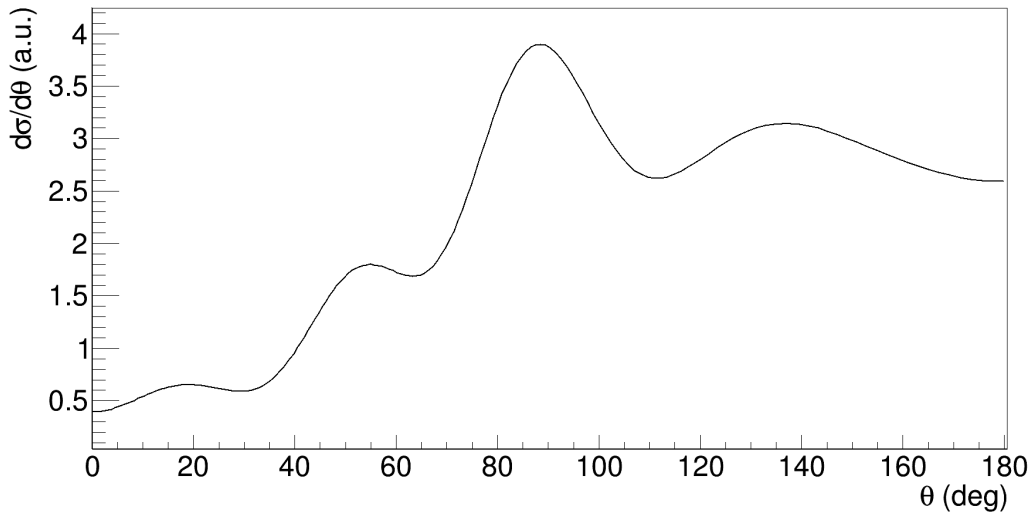

Figure 6.5: Angular distribution of neutrons emitted in the two-proton transfer reaction ^{64}Zn(^{3}He,n)^{66}Ge, for the population of the 2^+ state of ^{66}Ge at 957 keV.

first, and the event counts as if two neutrons had been detected in coincidence with each other. Interactions like these induce an error in the measurement of angular distributions, as neutrons are detected at angles they would not normally be at.
In order to counteract this phenomenon, angular distributions can be measured by considering only events where single neutrons are detected. This way, multiple coincident events caused by single neutrons scattering between different detectors are discarded.
Nonetheless, this does not completely solve the problem. It might happen that in the first interaction the amount of energy released by the neutron is below the threshold of the detector, and the interaction is not recorded. If the following interaction, or any other interaction after that, is the only one to be detected, then the neutron will be considered as if it was emitted at an angle that it was not. Again, this can induce an error in the measured distribution.

However, the angular distributions measured in fusion evaporation reactions show that the data points follow the expected trends. This suggests that the scattering of neutrons between different detectors, if present, is negligible and does not have a significant impact on the measurements.
Unfortunately, the attempt at measuring the angular distribution of neutrons emitted in the two-proton transfer reaction ^{64}Zn(^{3}He,n)^{66}Ge was not successful. The statistics are too low to perform the measurement: the data points do not follow the expected trend, and no information regarding the angular momentum of the populated state can be obtained. However, the fact that the experiment only lasted 22 hours needs to be kept in mind.

Chapter 7

Structure of ^{74}Se

Many nuclei were produced in the fusion evaporation reaction of the ^{64}Zn with the contaminants present in the target. In particular, the nucleus ^{74}Se was produced abundantly in fusion evaporation reactions with both ^{12}C (two protons evaporated) and ^{16}O (two protons, one α particle evaporated). With the collected data, the structure of this nucleus was studied.

The interest in its study comes from the fact that it is located at the border of a region known to show shape coexistence, a phenomenon where a particular atomic nucleus exhibits eigenstates with different shapes [26]. Middle mass nuclei with $N \sim Z$ in the Se-Br-Kr region are well known to display a variety of shapes [27–29]. However, the barriers between the competing shapes are often quite low, especially at low spin, so there is a considerable mixing of wavefunctions and the notion of the lowest states having simple shapes is often misconceived. The study of these middle mass nuclei, aimed at a complete spectroscopy of all the low lying states, can lead to a better understanding of the configuration mixing and of the barriers between the competing shapes.

The structure of ^{74}Se has been interpreted in many different ways over the years. In the most recent work [30], excited states in ^{74}Se where populated following the ε/β^+ decay of ^{74}Br, and a level scheme up to spin 6 was built up. In that publication, the low-lying states of ^{74}Se were interpreted as a set of near-spherical vibrational levels mixing strongly with prolate deformed states which have an unperturbed bandhead near 1350 keV.

In this thesis the level scheme of ^{74}Se will be discussed and the moment of inertia of the rotational band built on the yrast 4^+ state at 1363 keV will be discussed.

7.1 Level scheme

Only γ rays in coincidence with at least two protons detected by EUCLIDES were considered. The γ spectrum thus obtained only shows the transitions between the levels, so in order to understand the order of the transitions, γ-γ coincidences where exploited: when gating on a γ transition from a certain initial energy level, all the transitions feeding into that level appear of lower intensity; on the other hand, transitions from levels directly below the initial one have the same intensity; lastly, if a transition that appears while gating on a lower transition then disappears when gating on a higher one, the corresponding level finds itself on a different excitation band than the two levels used for the gates. By

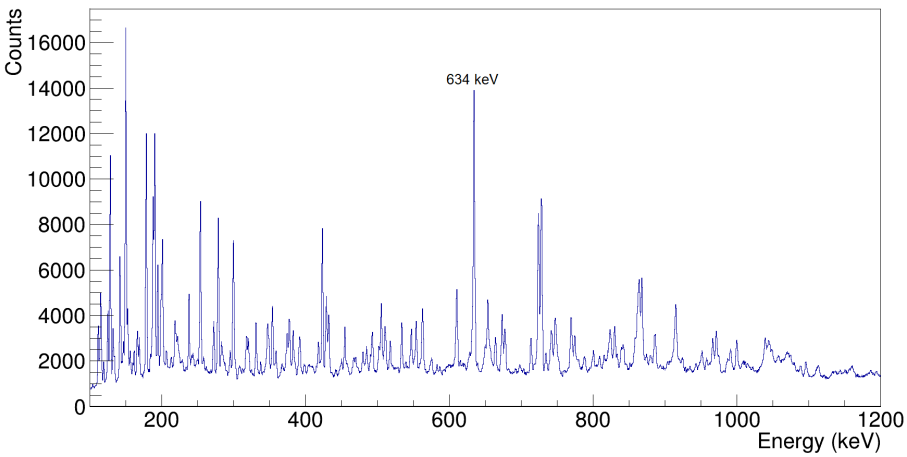

Figure 7.1: γ-ray spectrum in coincidence with at least two protons. The peak at 634 keV, corresponding to the $2_1^+ \rightarrow 0^+$ and $2_2^+ \rightarrow 2_1^+$ transitions of ^{74}Se, is highlighted.

performing these comparisons over and over after gating on many different transitions, it is possible to determine the order of all of the observed transitions. From this, the energy of the levels and the band structure of the excited states can be reconstructed.
In principle, the angular momentum of the excited states could also be measured from the angular correlations of the γ-ray transitions, which give information on the multipolarity of the radiation. In the case of this study, however, once the energy of the levels was reconstructed their angular momentum was assigned by comparing them with previously established assignments made in other works [30, 31].

During the analysis, the un-gated γ-ray spectrum including only γ rays in coincidence with at least two protons was first considered. Figure 7.1 shows such spectrum, where the peak at 634 keV, corresponding to the $2_1^+ \rightarrow 0^+$ and $2_2^+ \rightarrow 2_1^+$ transitions of ^{74}Se, is visible along many others not related to the nucleus. In order to detect only γ rays relative to the transitions of ^{74}Se, an additional gate in the γ-γ coincidence matrix was placed on the 634 keV peak. The resulting spectrum can be seen in Figure 7.2. In this spectrum, several transitions related to ^{74}Se could be observed.
From this, additional gates on higher transitions at 492 keV, 728 keV, 777 keV, 839 keV and 868 keV were used, with the purpose of comparing the intensities of the peaks and determine the order of the transitions. Moreover, these additional gates allowed the observation of less intense transitions that were submerged by the background in the γ-ray spectrum gated on the transition at 634 keV. The γ-ray spectra gated at the energies mentioned above are shown in Figures 7.3, 7.4, 7.5, 7.6 and 7.7.

The reconstructed level scheme is shown in Figure 7.8, while the measured transitions and the populated levels are described in detail in Table 7.1. The results are in agreement with previous works [30, 31].
^{74}Se was indeed produced abundantly during the experiment, but the statistics were still quite low. Nonetheless, the effort went mainly into trying to reconstruct, at least partially, the main bands of excited levels. Not all of the known transitions were visible: in particular, inter-band transitions and really high angular momentum levels were not measurable. The lowest relative intensity that was measured is 0.8: some transitions with lower intensities seemed to be present in the γ-ray spectra, but could hardly be distinguished from the background, so they were discarded in the analysis. Therefore, this value can be considered the lower measurement limit for this experiment.

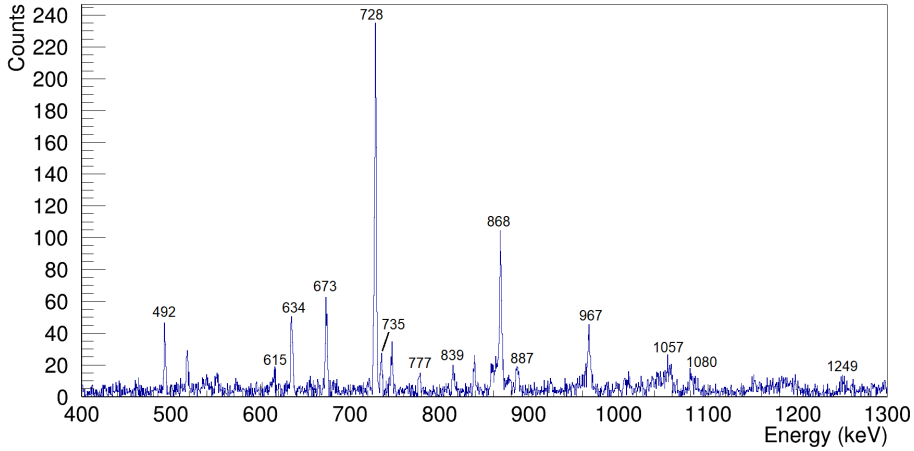

Figure 7.2: γ-ray spectrum in coincidence with at least two protons and with a gate the transition at 634 keV.

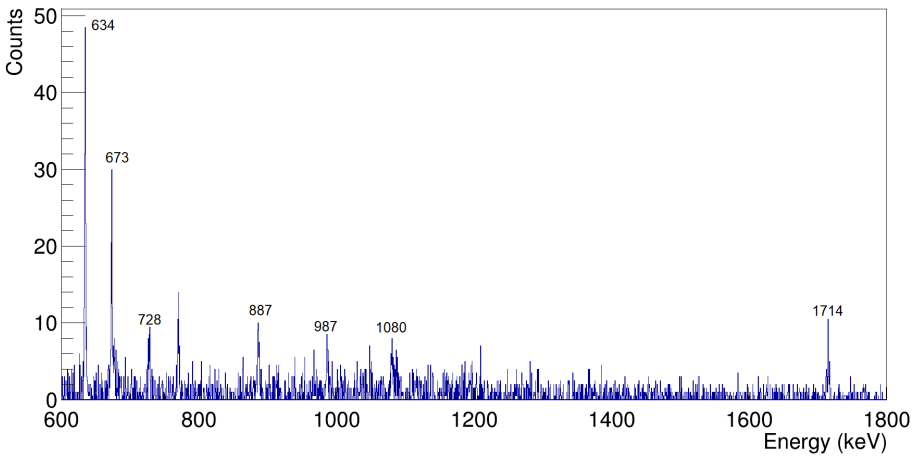

Figure 7.3: γ-ray spectrum in coincidence with at least two protons and with a gate on the transition at 492 keV.

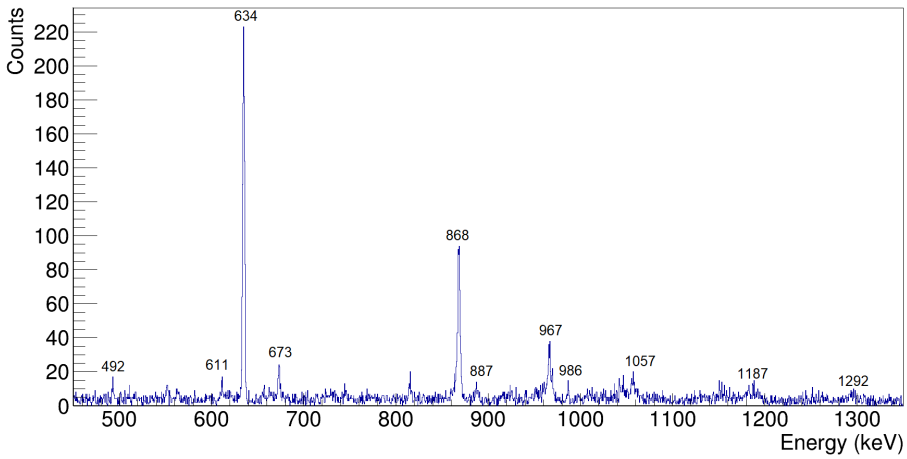

Figure 7.4: γ-ray spectrum in coincidence with at least two protons and with a gate on the transition at 728 keV.

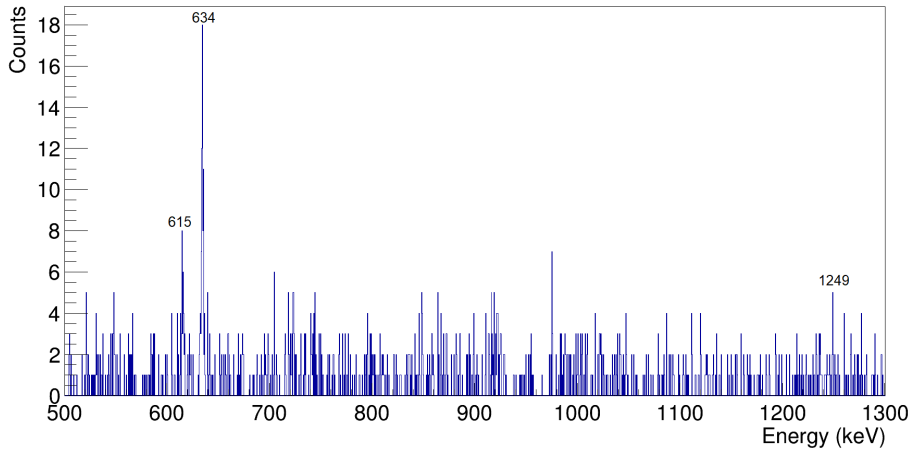

Figure 7.5: γ-ray spectrum in coincidence with at least two protons and with a gate on the transition at 777 keV.

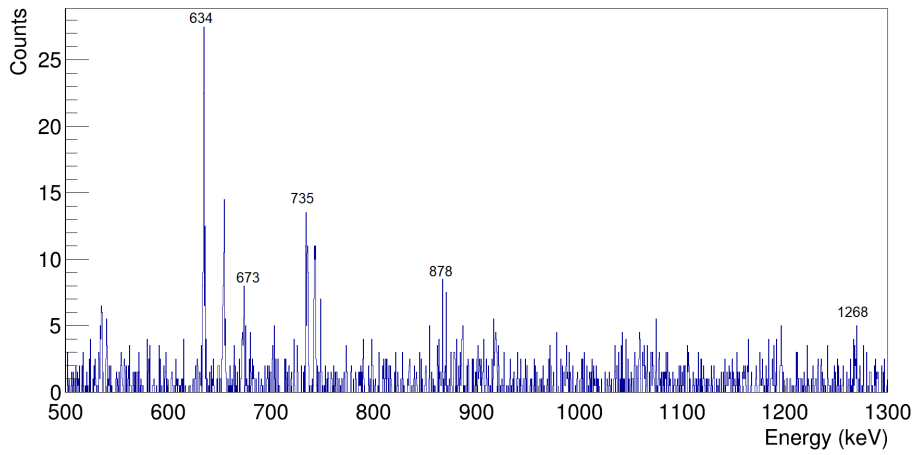

Figure 7.6: γ-ray spectrum in coincidence with at least two protons and with a gate on the transition at 839 keV.

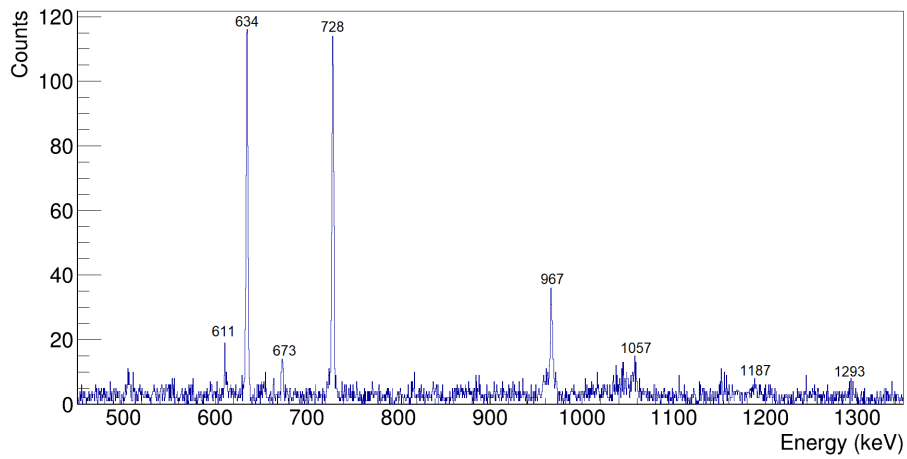

Figure 7.7: γ-ray spectrum in coincidence with at least two protons and with a gate on the transition at 868 keV.

J_i^π	E_i (keV)	J_f^π	E_f (keV)	E_γ (keV)	I_γ
2^+	634.82 (3)	0^+	0.00	634.82 (3)	100
2^+	1268.2 (9)	0^+	0.00	1268.2 (9)	4.8 (9)
		2^+	634.82	634.74 (8)	13.6 (9)
4^+	1363.23 (4)	2^+	634.82	728.41 (3)	56.9 (9)
3^+	1883.7 (9)	2^+	634.82	1249.5 (5)	1.1 (4)
		2^+	1268.2	615.4 (2)	1.1 (4)
4^+	2107.3 (9)	2^+	1268.2	839.1 (1)	5.4 (7)
6^+	2231.31 (6)	4^+	1363.23	868.08 (5)	36 (2)
3^-	2349.2 (4)	2^+	634.82	1714.4 (4)	2.3 (9)
		2^+	1268.2	1080.6 (3)	0.8 (4)
		4^+	1363.23	986.9 (5)	1.8 (6)
5^+	2661.2 (9)	3^+	1883.7	777.5 (2)	3.5 (4)
5^-	2842.2 (9)	4^+	2107.3	734.9 (1)	4.9 (6)
		6^+	2231.31	611.1 (3)	0.8 (2)
		3^-	2349.2	492.9 (2)	7.1 (8)
6^+	2985.7 (14)	4^+	2107.3	878.4 (11)	1.7 (6)
8^+	3198.2 (1)	6^+	2231.31	966.85 (9)	17 (1)
7^-	3515.5 (9)	5^-	2842.2	673.3 (1)	14.1 (3)
10^+	4255.5 (4)	8^+	3198.2	1057.3 (4)	9 (2)
9^-	4402.6 (9)	7^-	3515.5	887.1 (2)	6 (1)
12^+	5442.8 (7)	10^+	4255.5	1187.3 (6)	5 (1)
14^+	6735.4 (8)	12^+	5442.8	1292.6 (4)	1.2 (3)

Table 7.1: Levels populated in ^{74}Se following the ^{64}Zn+^{12}C and ^{64}Zn+^{16}O fusion evaporation reactions. Relative intensities for γ transitions depopulating the levels are given: I_γ is the measured intensity normalized to the intensity of the $2_1^+ \rightarrow 0_1^+$ ($I_{2_1^+\rightarrow 0_1^+} = 100$).

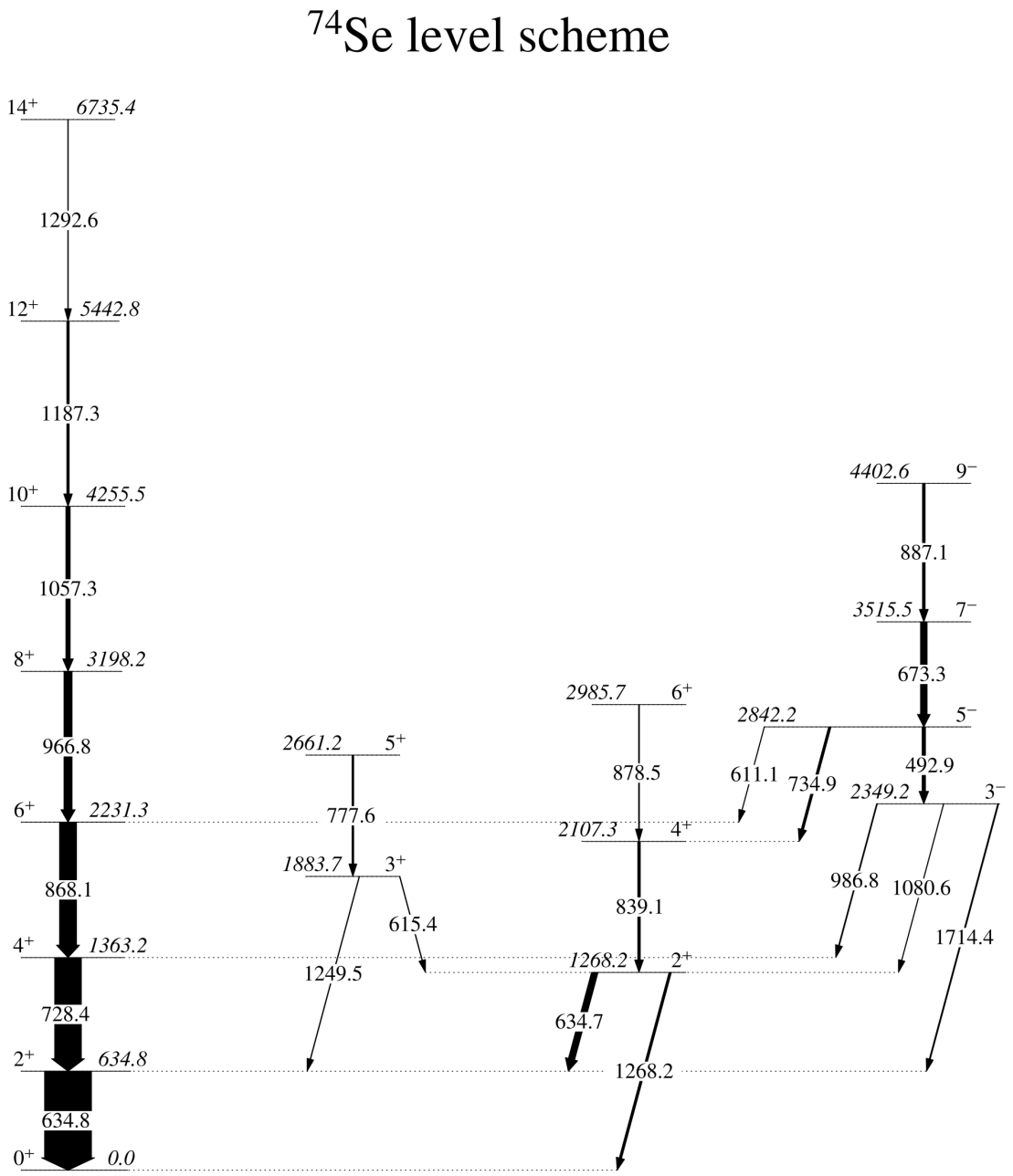

Figure 7.8: Reconstructed level scheme of ^{74}Se. The energies of the transitions and of the levels are reported in keV.

7.2 Moment of inertia of the yrast band

Much like a rotating classical object, a deformed, rotating atomic nucleus possesses a moment of inertia. The analogy, however, stops here, as the latter is a quantum system: the moment of inertia of a rotational excited state does not only depend on the mass distribution, but also on pairing correlations between nucleons, which is a purely quantum property.

In quantum mechanics, for a rigid rotor with hamiltonian

$$H = \hbar^2 \frac{I^2}{2J} \tag{7.1}$$

where I is the total angular momentum of the state and J is the moment of inertia, the moment of inertia can be related to the excitation energy of rotational states:

$$E = \frac{\hbar^2}{2J} I(I+1) \tag{7.2}$$

From this, the energy difference between a level and the level below, which corresponds to the energy of emitted (or absorbed) γ rays, is

$$\Delta E_{I,I-2} = E_\gamma = \frac{\hbar}{J}^2 (2I-1) \tag{7.3}$$

which gives

$$\frac{J}{\hbar^2} = \frac{2I-1}{E_\gamma} \tag{7.4}$$

The result is a linear relation between the energy of the γ rays emitted in the de-excitation of the states and the angular momentum of the states themselves. This holds only if J is constant along the whole band of rotational states, but in reality J depends on several parameters, such as deformation of the nucleus and pairing effects. This can mainly be observed in high angular momentum states, where it can also occur that J is smaller than for lower angular momentum states, causing the appearance of the so-called "backbending" phenomenon.

In the case of ^{74}Se, no backbending has been observed in previous works [31]. In this work, only the yrast band was observed up to high spin levels (14). The moment of inertia of each level was evaluated using the relation in equation 7.4 even though, in principle, this is valid only for a rigid rotor, and the result is shown in Figure 7.9. The calculation was made starting at the 4^+ level at 1363 keV, since it is the bandhead of an unperturbed rotational band. As anticipated, the trend is not linear, but no backbending is present, which is in agreement with previous measurements [31].

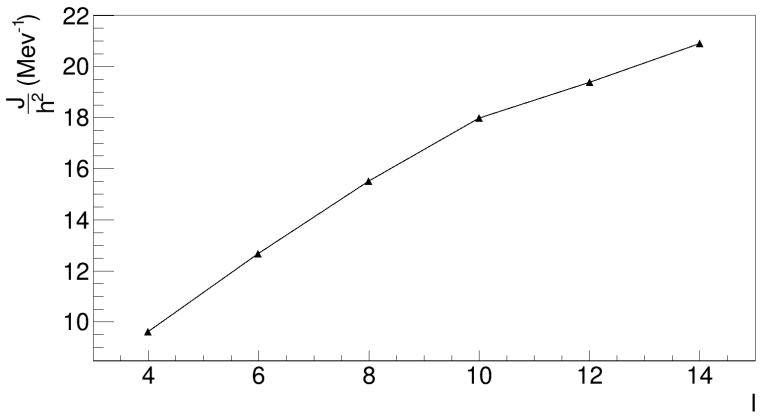

Figure 7.9: Moment of inertia of the rotational excited states in the yrast band of ^{74}Se, as a function of the angular momentum of the states.

Chapter 8

Conclusions

In this thesis, the test of a new ^{3}He target, produced with an innovative technique that provides a density of ^{3}He higher than other thin ^{3}He targets produced via implantation techniques, was performed. During the test, two identical targets were used for 11 hours each; a beam of ^{64}Zn was used for the test.

A visual examination of the target at the end of the experiment showed minimal signs of damage caused by the beam.
In order to check whether evaporation of ^{3}He from the target had occurred, the counting rate of ^{3}He nuclei, emitted from the target due to elastic scattering with the beam and detected in the front facing detectors of EUCLIDES, was analyzed. From this, it was possible to observe that after 11 hours (during which the beam intensity was varied between 2.3 pnA and 5 pnA) the density of ^{3}He inside the target had decreased by a factor of ~ 3. The only possible explanation for this is the evaporation of ^{3}He from the target. This phenomenon depends on the temperature reached by the target during the experiment, which in turn is related to the intensity of the beam. Considering that the target is to be used in combination with RIBs, which have very low intensities, this result shows that for such applications, the evaporation of ^{3}He from the target should not be a concern.
Instead, the main problem of the target is the presence of contaminants: they make up $\sim 28\%$ of the target, and their presence cannot be ignored. In fusion evaporation reactions with the beam, they cause an increase in background events, which can make detecting rare events (such as those from transfer reactions) harder or even impossible.

Still, while these contaminants would have a negative impact on an actual experiment, they allowed for further analysis to be done: by analyzing fusion evaporation channels, it was possible to perform a first time measurement of neutron angular distributions with the Neutron-Wall array. In particular, in fusion evaporation reactions of ^{64}Zn with ^{16}O present in the target, ^{77}Kr (evaporation of 2 protons and 1 neutron) and ^{77}Rb (evaporation of one proton and two neutrons) were produced. The angular distributions of neutrons detected in coincidence with γ rays emitted by these two nuclei were measured, and the results are in agreement with the expected values. Before doing the measurement, one of the concerns was the impact of neutrons scattering between different detectors, which could lead to the measurement of wrong distributions. However, the results obtained in the measurements suggest that this phenomenon, if present, has a negligible effect.

Given the results obtained from fusion evaporation reactions, an attempt was made at measuring the angular distribution of neutrons emitted in the two-proton transfer reaction

^{64}Zn(^{3}He,n)^{66}Ge. In particular, neutrons in coincidence with the γ transition of ^{66}Ge at 957 keV were considered. This measurement could give information on the angular momentum of the populated state in the final nucleus. However, the amount of detected γ rays corresponding to the transition of interest was low, and the amount of detected neutrons in coincidence with them was not sufficient to allow the measurement of the angular distribution.

The nucleus ^{74}Se, which belongs to a region of nuclei known to show shape coexistence, was populated in fusion evaporation reactions of ^{64}Zn with contaminants present in the target. Data acquired during the experiment allowed for the partial reconstruction of its level scheme, and for the measurement of the moment of inertia of the rotational excited states in the yrast band.

All of the results presented are in agreement with previous studies and expected values, but the errors are sometimes quite large. It is important to remember that the work presented here is the analysis of a test experiment which lasted for 22 hours and was aimed at testing the new ^{3}He target: actual experiments typically span over several days, so the data collected is much more abundant.

8.1 Future perspectives

The problem of the presence of contaminants in the target is already being addressed: the CSIC-Materials Science Institute of Seville, which originally manufactured the target, is working to increase the concentration of ^{3}He up to 10^{18} at/cm^{2} (currently $2.86 \cdot 10^{17}$ at/cm^{2}), while simultaneously decreasing the concentration of contaminants below 5%. This new version of the target should be ready by the end of 2018.

An additional improvement that could be done for experiments that make use of this target, this time regarding the measurement of neutron angular distributions, would be the use of a more advanced neutron detector. One example could be the NEutron Detector Array, NEDA [32], which is an international project currently under development. Compared to Neutron-Wall, NEDA will provide higher detection efficiency, better neutron-γ ray discrimination and higher angular resolution. All these elements would allow NEDA to measure neutron angular distributions with greater accuracy with respect to what was done in this work with Neutron-Wall.

In the meantime, two experiments which make use of the target have already been planned. The first one, which has already been approved, will be performed at the LNL: its aim is to study the low-lying states in the doubly magic nucleus ^{56}Ni by populating them in the reaction ^{54}Fe(^{3}He,n)^{56}Ni. The second one has been proposed at GANIL in Caen, France: its goal is to measure the Colossal Mirror Energy Differences [33] between the neutron-deficient ^{36}Ca and its mirror nucleus ^{36}S; ^{36}Ca will be produced in the reaction ^{34}Ar(^{3}He,n)^{36}Ca.

Bibliography

[1] A. Fernandéz, V. Godinho, D. Hufschmidt, M. C. Jiménez de Haro (patent pending).

[2] B. Cederwall et al., Nuclear Instruments and Methods in Physics A 354 (1995) 591-594.

[3] J. J. Valiente-Dobón et al., LNL-INFN Annual Report 2014, 95.

[4] Ö. Skeppstedt et al., Nuclear Instruments and Methods in Physics Research A 421 (1999) 531-541.

[5] D. Testov et al., LNL-INFN Annual report 2015, 105.

[6] H. Feshbach, "Transfer Reactions" in *Theoretical Nuclear Physics, Nuclear Reactions.*

[7] F. Zardi, "Reazioni di trasferimento " in *Teoria delle collisioni fra ioni pesanti, Parte II - Le collisioni radenti.*

[8] R. P. J. Winsborrow, B. E. F. Macefield, Nuclear Physics A 182 (1972) 481-496.

[9] Th. Blaich et al., Nuclear Instruments and Methods in Physics Research A314 (1992) 136-154.

[10] SIAM Platform website: `platforms.unamur.be/platforms/siam`.

[11] R. G. Milner et al., Nuclear Physics A 497 (1989) 495c–508c.

[12] S. Kato et al., Nuclear Instruments and Methods in Physics Research A 307 (1991) 213-219.

[13] W. H. Geist et al., Nuclear Instruments and Methods in Physics Research B 111 (1996) 176-180.

[14] R. T. Kouzes, *The* ^{3}*He Supply Problem*, PNNL-18388 (2009).

[15] A. Lombardi et al., LNL-INFN Annual Report 2014, 95.

[16] G. Fortuna et al., Nuclear Instruments and Methods in Physics Research A 287 (1990), 253.

[17] Z. Kis et al., Nuclear Instruments and Methods in Physics Research A 418 (1998) 374-386.

[18] B. Fazekas et al., Proceedings of the 4th International Conference on Methods and Applications of Radioanalytical Chemistry, Kailua-Kona, Hawaii, USA, April 1997.

[19] RadWare code website: `https://radware.phy.ornl.gov`.

[20] I. Zanon, *Study of Shape Coexistence in the* ^{188}*Hg nucleus via lifetime measurements*, Master's thesis, University of Padova, 2018.

[21] P.-A. Söderström et al., Nuclear Instruments and Methods in Physics Research A 594 (2008) 79-89.

[22] C. Fransen, private communication.

[23] National Nuclear Data Center - Brookhaven National Laboratory `https://www.nndc.bnl.gov`.

[24] A. Di Nitto, extensively modified version of the original code LILITA written by J. Gomez del Campo and R. G. Stockstad, Oak Ridge National Laboratory, Report No. TM7295, `http://web.ornl.gov/info/reports/1981/3445605518062.pdf`, unpublished.

[25] M. Igarashi, J. Tostevin, Computer Program TWOFNR (Surrey University version), private communication.

[26] Review of Modern Physics 83, 1467 (2011).

[27] E. Clément et al., Physical Review C 75, 054313(2007).

[28] J. Ljungvall et al., Physical Review Letters 100, 102502 (2008).

[29] C. Plettner et al., Physical Review Letters 85, 2454 (2000).

[30] E. A. McCutchan et al., Physical Review C 87, 014307 (2013).

[31] J. Döring et al., Physical Review C 57, 2912 (1998).

[32] J. J. Valiente-Dobón et al., *NEDA - NEutron Detector Array* (2018). Preprint submitted for publication.

[33] J. J. Valiente-Dobón et al., Physical Review C 98, 011302(R) (2018). by caring for me

Acknowledgements

I would like to express my sincere gratitude to Dr. Daniele Mengoni and Dr. Jose Javier Valiente-Dobón, for giving me the opportunity to work on this project and sharing with me their knowledge and suggestions, to Dr. Marco Siciliano, for the immense help that he gave me during the thesis and for the good talks that we had, and finally to all of the other members of the Gamma group at the Legnaro National Laboratories, who were always helpful in answering my questions and doubts. I am really glad I could be part of such a lively group.

Many thanks also go to Prof. Asunción Fernández, Dr. Vanda Godinho, Mr. Dirk Hufschmidt and Dr. Maria del Carmen Jiménez de Haro of the CSIC Materials Science Institute of Seville, who provided the ^{3}He target that was tested in this experiment.

Finally, I must express my gratitude to my parents, for providing me with their unwavering support and encouragement throughout my years of study, and to my girlfriend, who by always being by my side and caring for me prevented my descent into madness during the last few months of working on this project.